AD-A278 010

SC71061.FR

Copy No. 8

SC71061.FR

Quantum Well Infrared Photodetector FPA

FINAL REPORT

September 1, 1991 through February 28, 1993

CONTRACT NO. N00014-91-C-0163

Prepared for:

Scientific Officer
Office of Naval Research
800 N. Quincy Street
Arlington, VA 22217-5000
Attn: Max Yoder

DTIC
ELECTE
APR 0 [illegible]
S G D

Prepared by:

L. Kozlowski
Rockwell International Science Center

MARCH 1994

94-09412

Approved for public release

Rockwell International
Science Center

94 3 25 104

REPORT DOCUMENTATION PAGE

Form Approved
OMB No. 0704-0188

Public reporting burden for this collection of information is estimated to average 1 hour per response, including the time for reviewing instructions, searching existing data sources, gathering and maintaining the data needed, and completing and reviewing the collection of information. Send comments regarding this burden estimate of any other aspect of the collection of information, including suggestions for reducing this burden, to Washington Headquarters Services, Directorate for Information Operations and Reports, 1215 Jefferson Davis Highway, Suite 1204, Arlington, VA. 22202-4302, and to the Office of Management and Budget, Paperwork Reduction Project (0704-0188), Washington, DC 20503

1. AGENCY USE ONLY *(Leave Blank)*	2. REPORT DATE	3. REPORT TYPE AND DATES COVERED
	MARCH 1994	Final 09/01/91 - 02/28/1993

4. TITLE AND SUBTITLE

Quantum Well Infrared Photodetector FPA

5. FUNDING NUMBERS

4. AUTHOR(S)

L. Kozlowski

7. PERFORMING ORGANIZATION NAME(S) AND ADDRESS(ES)

Rockwell International Science Center
P.O. Box 1085
Thousand Oaks, CA 91358

7. PERFORMING ORGANIZATION REPORT NUMBER

SC71061.FR

9. SPONSORING / MONITORING AGENCY NAME(S) AND ADDRESS(ES)

Scientific Officer
Office of Naval Research
800 N. Quincy Street
Arlington, VA 22217-5000

9. SPONSORING / MONITORING AGENCY REPORT NUMBER

NTIS CRA&I X
DTIC TAB
Unannounced
Justification

By
Distribution /

11. SUPPLEMENTARY NOTES

12a. DISTRIBUTING/A

Statement A per telecon Max Yoder
ONR/Code 1114
Arlington, VA 22217-5000

NWW 4/7/94

12b. DISTRIBUTION CODE

Dist	Avail and/or Special
A-1	

13. ABSTRACT *(Maximum 200 Words)*

The AT&T/Rockwell team met all the objectives of this collaborative program; AT&T supplied the QWIP detector arrays and Rockwell subsequently fabricated hybrid focal plane arrays using available high performance CMOS multiplexers, tested the hybrids, performed breadboard imaging demonstrations and delivered several hybrid FPAs. Eighteen hybrids were fabricated and evaluated. The collaboration yielded significant improvements in QWIP FPA performance and reliability and many milestones including:

- first BLIP LWIR FPA sensitivity demonstration at low photon backgrounds ($<10^{12}$ photons/cm^{2}sec) with the GaAs-based quantum well infrared photodetector (QWIP) technology.
- high LWIR FPA pixel operability.
- NEΔT's as low as 5 mK at LWIR imaging backgrounds at f/1.4 and temperatures consistent with mechanical coolers (~ 65K)
- increased coupling efficiency by over an order of magnitude; achieved effective quantum efficiency of ~ 10% with low crosstalk.
- effective quantum efficiencies of up to 30% under flood illumination, though with high crosstalk.
- mean D* of 10^{14}cm-Hz$^{1/2}$/W at 3.0 x 10^9 photons/cm^2-sec background at 32.5K operating temperature with > 98% operability.
- maximum temperature for 9.5 μm FPA BLIP sensitivity as high as 62K.
- excellent hybrid reliability by mechanically thinning the QWIP.
- responsivity nonuniformity < 3% rms, thus enabling >83 dB dynamic range.

14. SUBJECT TERMS

15. NUMBER OF PAGES

76

16. PRICE CODE

17. SECURITY CLASSIFICATION OF REPORT	18. SECURITY CLASSIFICATION OF THIS PAGE	19. SECURITY CLASSIFICATION OF ABSTRACT	20. LIMITATION OF ABSTRACT
UNCLASSIFIED	UNCLASSIFIED	UNCLASSIFIED	UL

NSN 7540-01-280-5500
F-0045-SC

Standard Form 298 (Rev. 2-89)
Prescribed by ANSI Std Z39-18 298-102

Table of Contents

Page

1.0 Introduction 1

1.1 Synopsis 1
1.2 Highlights 4
1.3 Background 6

2.0 Detector Performance Tests 8

2.1 Layer 1195 10

2.1.1 Low Background Measurements 11
2.1.2 High Background Measurements 17
2.1.3 Summary 22

2.2 Impact of Optical Coupling Improvements on Discrete Detector Performance 23
2.3 Summary of Layer 1285 and Layer 1286 Detectors 29

3.0 CMOS Readouts 31

3.1 High Capacity Direct Injection Readout 31
3.2 Gate Modulation Readout 33
3.3 Electronically Scanned Buffered Direct Injection Readout 36

4.0 QWIP Hybrid FPA 39

4.1 Architecture 39

5.0 Hybrid FPA Performance 40

5.1 Impact of Optical Coupling Improvements 40
5.2 Low Background 44
5.3 FPA Performance at Conventional Imaging Backgrounds 48

5.3.1 Layer 1195 FPA Performance 48
5.3.2 Impact of Optical Coupling Improvements 57

6.0 FPA Test Methodology 60

6.1 Test Plan 60
6.2 Test Station Electronics 61

7.0 QWIP FPA Cost Summary 64

8.0 References 66

List of Figures

Figure		Page
1	D* vs. temperature for AT&T/Rockwell 128 x 128 FPAs	4
2	GaAs/AlGaAs QWIP detector cross section	9
3	Spectral Response for Layer 1195	11
4	Cumulative distribution function of R_0A products at 78K for layer 1195	12
5	I-V characteristics on linear scales of three detectors at 78K; the curves are extremely close at all bias voltages	12
6	I-V characteristics vs. temperature from 100K to 11K	13
7	Layer 1195 dark current at selected bias voltages vs. inverse temperature	14
8	Layer 1195 activation energy data extracted from forward (positive with respect to substrate) and negative bias voltages	15
9	Layer 1195 noise as a function of bias and temperature	16
10	Layer 1195 photoconductive gain	16
11	Layer 1195 detector I-V's under high background	17
12	Layer 1195 detector noise vs. temperature under high background	18
13	Layer 1195 photoconductive gain vs. temperature under high background	19
14	Layer 1195 responsivity vs. bias at 8K and 78K	19
15	Layer 1195: Determination of optically active area	21
16	Quantum efficiency active area product for 11 detectors	21
17	Layer 1195 detector-limited D* vs. reciprocal temperature	23
18	Comparison of 78K I-V characteristics for four wafer samples	25
19	Focused spot measurement system	26
20	Comparison of responsivity measurements	26
21	Focused spot measurement showing excess signal generated by crosstalk at FPA level	27

List of Figures (Cont'd)

Figure		Page
22	Comparison of high temperature dark current and high background photocurrent	28
23	Zero field-of-view D* vs. temperature	29
24	128 x 128 High Capacity Direct Injection Readout	32
25	128 x 128 Readout With Gate Modulation Input and CMOS Switched-FET Readout Architecture	33
26	Block Diagram of ESBDI readout	37
27	Cross sectional illustrations of the hybrid focal plane array comprised of the detector array and the CMOS readout, and the quantum well infrared detector array	39
28	Histogram of ηC_p and $\eta C_p G$ for Hybrid FPA B-08	40
29	Array Map for FPA B-08 showing optical crosstalk peaks of 5% along both axes of the 2-D optical grating for focused spot illumination	41
30	Photoconductive gain vs. detector bias for layer 1289	43
31	$\eta C_p G$ for Hybrid B-03 with 1-D lamellar grating at 0.8 V and 1.4 V bias	43
32	Peak D* histograms at 40K and 35K operating temperatures for QWIP FPA from wafer #1 at 1.29 x 10^{10} photons/cm^2-s background	44
33	Current-Voltage traces from layers 1195 (a) and 1242 (b) measured at zero degree field-of-view with the detector looking at 20–30K background	45
34	Histogram of the peak D* measured at 1.68 x 10^{11} photons/cm^2-s background and 40K temperature for layer 1242	46
35	Histogram of the peak D* measured at 3.0 x 10^9 photons/cm^2-background and 32.5K temperature (Thinned; Layer 1289)	47
36	D* vs. background flux	47
37	D* vs. 1000/T for tactical operating temperatures and 22.5 ms integration time	50
38	D* at 22.5 ms integration time and 77K operating temperature	50
39	G-R limited D* at 77K (510 µs integration time)	51

List of Figures (Cont'd)

Figure		Page
40	Johnson noise limited NEΔT at 77K and 22.5 msec integration time	51
41	BLIP D* for Hybrid B-002 (1.5 x 10^{16} photons/cm^2-s background)	52
42	BLIP NEΔT for f/1.6 illumination and ~ 50 Hz frame rate	52
43	$\eta \cdot C_p \cdot G$ nonuniformity for Grade "B" Hybrid B-002	53
44	$\eta \cdot Cp \cdot G$ nonuniformity at 0.8V for Grade "A" Hybrid B-003	54
45	$\eta \cdot Cp \cdot G$ nonuniformity at 1.4 V for Grade "A" Hybrid B-003	55
46	Array map showing crosstalk pattern for spot scan illumination	56
47	Layer 1289 D* histogram obtained at 1 x 10^{16} photons/cm^2-s background and 60K temperature	58
48	Layer 1289 NEΔT histogram generated at 1 x 10^{16} photons/cm^2-s background and 60K temperature	58
49	Mean D* vs. background flux at 40K for several thinned and unthinned hybrids using detector arrays from layers 1195 (#1), 1242 (#2) and 1289 (#3)	59
50	FPA test setup	62
51	Interface Electronics schematic (typical)	62
52	IR&D 128 x 128 multiplexer wafer floor plan showing the four devices developed simultaneously in fiscal year 1988	64

Tables

Table		Page
1	QWIP FPA Performance Summary	3
2	Comparison of QWIP Discrete Detector Performance	24
3	Comparison of Layers 1285, 1286, and 1289	30
4	High Capacity Direct Injection Readout Characteristics	32
5	Gate Modulation 128 x 128 Multiplexer Characteristics	36
6	ESBDI Multiplexer Characteristics	38
7	QWIP FPA Quantum Efficiency	42
8	Lot 1 QWIP FPA Performance	48
9	Lot 1 QWIP FPA Performance Summary	53
10	Lot 1 QWIP FPA Nonuniformity	54
11	Detector 1/f Noise Comparison	55
12	FPA Performance Summary at 78K	57
13	Gate Modulation Readout: Interface Electronics	63
14	QWIP FPA Cost Analysis	65
15	IR&D 128 x 128 Readout: Typical Functional Yield	65

1.0 Introduction

1.1 Synopsis

This final report is submitted in successful completion of Rockwell's effort supporting the Quantum Well Infrared Photodetector (QWIP) Focal Plane Arrays for Staring IR Sensor Systems program. The AT&T/Rockwell team met all the objectives of this collaborative program; AT&T supplied the QWIP detector arrays and Rockwell subsequently fabricated hybrid focal plane arrays using available high performance CMOS multiplexers, tested the hybrids, performed breadboard imaging demonstrations and delivered several hybrid FPAs. Eighteen hybrids were fabricated and evaluated. The program objectives include:

- advancing the basic technology of staring GaAs/AlGaAs QWIP FPAs
- providing breadboard imaging demonstration in the long wavelength infrared (LWIR ~ 8-12 μm) spectral band
- assessing the manufacturability and cost of QWIP FPAs based on actual yield data and performance specifications

The program responsibilities were shared among AT&T, Rockwell and the Government. The detector arrays were fabricated by AT&T Bell Laboratories at the Solid State Technology Center, Breinigsville, PA.[18] Detector performance improvement work was also partially funded by S^3-Maxwell (Dr. J.D. Boisvert, San Diego, CA) for the Phillips Laboratory under Contract F29601-88-C-0025.

AT&T fabricated the GaAs/AlGaAs material and detector arrays in several advanced architectures. Rockwell provided the multiplexers, fabricated and tested the hybrid FPAs, and performed the imaging demonstrations. Mr. Ray Balcerak of ARPA funded the program. Mr. Max Yoder of the Office of Naval Research oversaw the program and several government-related users provided independent hybrid FPA evaluation via critical use of delivered FPAs. A device delivered to Kate Forrest of NASA/Goddard, for example, is providing insight into LWIR FPA usefulness for earth resource mapping.

AT&T exploited the maturity of molecular beam epitaxy to reproducibly grow the high quality IR-sensing materials. This maturity led to rapid progress in increasing the responsivity and detectivity of the quantum well infrared photodetectors (QWIPs) fabricated in the GaAs/AlGaAs material system. The AT&T/Rockwell collaboration produced results that are similar to those recently reported elsewhere[1-18] including factor of ~ 4 improvement in performance as discussed by Andersen[19] in GaAs/AlGaAs QWIPs using an AlAs waveguide design.[4,5] The increased responsivity should enable QWIP technology to address the needs of several infrared focal plane array (IRFPA) applications requiring moderate to high sensitivity. In conjunction with the QWIP's high producibility and uniformity, this progress has culminated in the development of focal plane arrays in 128 × 128 and 256 × 256 formats and the demonstration of high performance discrete detectors having either medium wavelength infrared ($\lambda \sim \mu m$)[12,13] or long wavelength infrared (LWIR $\lambda \sim 8$–$19\ \mu m$)[1-11,14-16] absorption. In the near future, the GaAs/AlGaAs material system will enable the growth of two- or multi-color detectors on the same substrate to provide spatially-coincident, wavelength-selective QWIPs.[17] The key remaining LWIR QWIP need is for yet higher performance at 80K.

QWIP FPA Summary. Table 1 summarizes the performance of the eighteen hybrids fabricated and subsequently evaluated over the course of the program. Key performance attributes include excellent low background sensitivity, ≈10% quantum efficiency with low crosstalk, and consistently high pixel operability at both low and high backgrounds.

The continuing improvements in quantum efficiency along with the uniform and low dark current of the GaAs/AlGaAs detectors confirm a niche for this detector technology at photon backgrounds $<10^{12}$ photons/cm^2-s and ≤40K operating temperature. Attainment of BLIP sensitivity at high backgrounds, however, presently falls short of the nominal goal of 80K; operating temperatures ≤65K are required for BLIP achieving BLIP sensitivity at conventional imaging backgrounds. Figure 1 summarizes the good FPA performance achieved at high temperature and background, and the excellent performance attained at low background and temperature.

Table 1

QWIP FPA Performance Summary

FPA	QWIP WAFER	MUX	ηC_p (%)	Φb (cm^{-2}-s)	TEMP (K)	OPERABILITY (%)	D* (Jones)
B-01	1189	HCDI	-	$2x10^{16}$		99.7	N.A.†
B-02	1189	HCDI	3.9	$1.95x10^{16}$	57	98.6	$1.12x10^{10}$
B-03	1189	HCDI	3.8	$1.95x10^{16}$	60	99.4	$1.16x10^{10}$
B-04	1242	HCDI	7.8	$2.06x10^{16}$	62	98.8	$3.01x10^{10}$
B-05	1242	GPN	9.2	$1.68x10^{11}$	40	99.4	$1.44x10^{13}$
B-06	1189	GPN	4.0	$1.2x10^{10}$	35	99.8	$4.51x10^{13}$
B-07	1289	HCDI	23	$2.26x10^{16}$	50	98.1	$6.39x10^{10}$
B-08	1289	HCDI	23	$2.26x10^{16}$	50	99.6	$6.67x10^{10}$
B-09	1289	GPN	-	-	-	BAD MUX	-
B-10	1289	GPN	8.0T	$3.0x10^{9}$	32.5	99.3	$9.96x10^{13}$
B-11	1286	HCDI	2.0T	$1x10^{16}$	40	98.5	$3.1x10^{10}$
B-12	1285	HCDI	4.0T	$1x10^{16}$	40	93.3	$9x10^{9}$
B-13	1285	HCDI	5.0T	$1x10^{16}$	≤58	>99.5	$2.2x10^{10}$
B-14	1289	HCDI	6.0T	$1x10^{16}$	≤58	>97	$4.0x10^{10}$
B-15	1289	ESBDI	11	$2x10^{16}$	58	-	$>1x10^{8}$‡
B-16	1289	HCDI	8.0T	$1x10^{16}$	≤62	>99.1	$7.9x10^{10}$
B-17	1286	HCDI	2.3	$1.5x10^{16}$	≤57	96.6	$2.5x10^{10}$
B-18	1285	HCDI	3.3	$1.5x10^{16}$	≤57	94.7	$2.7x10^{10}$

T-Mechanical thinned via diamond-point lathe
HCDI-High Capacity Direct Injection Readout; GPN- Gate Modulation Readout; ESBDI- Electronically Scanned Buffered Direct Injection Readout
† Data not available. Dewar window imploded during data acquisition.
‡ ESBDI Multiplexer proved nonoptimum due to its low integration duty cycle and low transimpedance

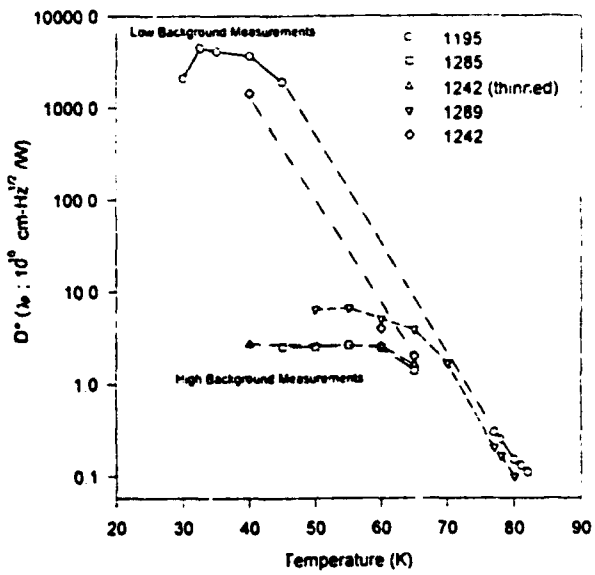

Fig. 1 D* vs. Temperature for AT&T/Rockwell 128 x 128 FPAs.

1.2 Highlights

The collaboration with AT&T yielded significant improvements in QWIP FPA performance and reliability. We achieved many milestones over the course of the program including:

- first demonstration of BLIP LWIR FPA sensitivity at low photon backgrounds ($<10^{12}$ photons/cm^2-sec) with the GaAs-based quantum well infrared photodetector (QWIP) technology.
- high LWIR FPA pixel operability at high *and* low backgrounds.
- NEΔT's as low as 5 mK at LWIR imaging backgrounds under f/1.4 illumination and temperatures consistent with mechanical coolers (≈65K)
- reasonable quantum efficiency of ~ 10% along with low crosstalk and high MTF.
- increased coupling efficiency by over an order of magnitude over the course of the program. We thus achieved effective quantum efficiency of ≈10% with low crosstalk.

- effective quantum efficiencies of up to 30% under flood illumination, though with high crosstalk.

- mean D* of 10^{14} cm-Hz1/2/W at 3.0 x 10^9 photons/cm^2-sec background at 32.5K operating temperature with > 98% operability.

- increased maximum temperature for 9.5 μm FPA BLIP sensitivity to as high as 62K.

- excellent hybrid reliability by mechanically thinning the QWIP (i.e., essentially removing the thick GaAs substrate).

- responsivity nonuniformity < 3% rms, thus enabling > 83 dB dynamic range.

9.5 μm (λ_c) 128 × 128 GaAs/AlGaAs multiple quantum well focal plane arrays (FPA) performance was significantly enhanced and their reproducibility was demonstrated. Among the key advancements in the state of the art included the first achievement of background-limited infrared photodetector (BLIP) sensitivity at low photon backgrounds (<10^{12} photons/cm^2-sec) with the GaAs-based quantum well infrared photodetector (QWIP) technology. Though high and nonuniform detector dark current often precludes this objective using other LWIR detector materials,[20] near-theoretical 128 × 128 FPA peak detectivity (D*) with > 99.4% pixel operability was achieved at 32.5 to 40K operating temperature at photon background as low as 3.0 x 10^9 photons/cm^2-sec. LWIR FPA D* of 1 x 10^{14} cm-Hz$^{1/2}$/W was, for example, attained at 32.5K operating temperature on a 128 × 128 device having a mechanically thinned backside-illuminated detector array with two-dimensional optical grating, AlAs waveguide layer and ~ 9.5 μm cutoff wavelength. We believe that this sensitivity is unprecedented for a staring LWIR FPA.

The sensitivities achieved with the fully optimized optical coupling structure were significantly superior to those achieved on earlier FPAs having only one-dimensional or two-dimensional optical gratings. The D* of QWIP hybrid FPAs having only 1-D grating, for example, had maximum value at background of approximately 1 x 10^{10} photons/cm^2-sec. Mean D* of 4.51 x 10^{13} cm-Hz$^{1/2}$/W was measured at 35K, which corresponds to 75% of BLIP for the measured effective quantum efficiency of ~ 1.0%. Pixel operability was very high, at 99.7%—an extraordinary result at low background. Mean D* of 3.2 x 10^{13} cm-Hz$^{1/2}$/W was measured at the 1.2 x 10^{10} photons/cm^2-sec background at 40K operating temperature.

Typical noise equivalent temperature difference of 5 to 8 mK and $D^* > 4 \times 10^{10}$ cm-$Hz^{1/2}/W$ were measured at conventional imaging backgrounds at up to 65K operating temperature. Also reported is progress in improving the effective quantum efficiency to about 10% with low optical crosstalk using two-dimensional gratings, resonant cavity structure and mechanical thinning.

The improved quantum efficiency and maintenance of uniform and low dark current should establish a niche for the GaAs/AlGaAs detectors technology for surveillance applications at photon backgrounds $< 10^{12}$ photons/cm^2-s and ~ 40K operating temperature. The ultra-low and uniform detector dark current at ≤ 40K is extremely attractive for nonimaging applications including long range object detection and surveillance at low photon backgrounds; at low background and operating temperature, the achievement of very low and uniform detector dark current is challenging for any LWIR detector technology. Incorporating the improvements achieved in the optical coupling using resonant optical cavities[21,22,23] should further enhance performance. Attainment of BLIP sensitivity at high backgrounds, however, presently falls short of the nominal goal of 80K; Operating temperatures ≤ 65K are required for BLIP sensitivity at conventional imaging backgrounds.

1.3 Background

Many IR FPA applications require array size, producibility, or low cost more than sensitivity. PtSi has been successful meeting some of these needs in the MWIR spectral band for applications compatible with 3.4 to 4.1 μm spectral bandpass. The long wavelength spectral region (LWIR; 7.5 to 12 μm) previously had no comparably mature technology. IrSi was investigated as a potentially cost-effective LWIR detector, but has dark current limitations that translate to the need for cooling well below the range of temperatures accessible via LN_2. We have thus evaluated quantum well infrared photodetectors (QWIP) in the GaAs/AlGaAs material system as a possible solution. The progression from single element, laboratory-based demonstrations to large field-tested staring arrays has been rapid.[24] The key milestone of yielding moderate sensitivity (≤ 50 mK) at 78K temperature has, however, not yet been achieved. The AT&T/Rockwell team has nevertheless achieved excellent performance at temperatures compatible with Stirling-cycle mechanical coolers.

Because of the extensive scientific and commercial exploration of the GaAs/AlGaAs material system, the application of QWIP technology to infrared detector array fabrication is well-

advanced. Although these detectors are inferior in D^* to intrinsic HgCdTe, advantages in controllability and yield are significant factors for producing large arrays. Competitive technologies to HgCdTe, such as PtSi and extrinsic silicon, are being developed because of these advantages; even though from fundamental considerations, HgCdTe is a superior and more uniform detector material system. In addition, GaAs/AlGaAs superlattice detectors have inherent advantages in both transient and total dose radiation hardness compared to HgCdTe detectors.

Possible disadvantages of the QWIP include its relatively low quantum efficiency and narrow-band spectral characteristics. Increasing the quantum efficiency mandates development of optimized optical gratings and resonant cavities. Another key limitation is the short lifetime translating to a need for lower operating temperatures than intrinsic detector materials. The operating temperature constraint is aggravated by the low quantum efficiency. However, the reported GaAs/AlGaAs quantum well detector performance generally approaches theoretical limits closer than intrinsic LWIR detectors such as $Hg_{1-x}Cd_xTe$. When coupled with readout-imposed charge-handling limitations, the devices are competitive for niche applications. Possible advantages in uniformity, controllability, and yield are also significant factors for producing large arrays.

Perhaps the most overwhelming motivator for the development of GaAs-based QWIP detectors is the synergy with mass market ventures where spin-off benefits translate to expedited resolution of materials development issues. High sensitivity IR FPA development focusing on materials such as HgCdTe has conversely been proceeding at a pace set primarily by government funded programs. Though seemingly copious amounts of DoD, BMDO (and previously SDIO) and NASA funds have been invested, the investments have nevertheless proved inadequate to produce high sensitivity LWIR detector technologies in volume at low cost, because LWIR detector fabrication is complicated by both the daunting technical challenge and the lack of synergy with commercial ventures that fuel demand. In stark contrast, silicon readout multiplexer technology has been able to exploit advancements in the state of the art fostered by the commercial memory market. Device architectures have thus moved from charge coupled devices to CMOS switched FET architectures that are similar to static RAMs. Rockwell has thus been able to develop complex readouts in formats up to 640 × 480 at sufficiently low cost to no longer be a significant factor in the recurring price of a deliverable hybrid.

2.0 Detector Performance Tests

Detector performance was measured on a discrete detector basis at Rockwell both to provide insight into FPA-level performance and to substantiate the AT&T test results. Many discrete measurements were performed on layers 1195, 1242, 1285, 1286 and 1289. These and other layers fabricated during the program were generally made with a standard structure that enabled direct comparison of the various optical coupling improvements implemented over the course of the program. The typical QWIP structure consisted of 40Å quantum wells (doped 10^{18} cm^{-3}) and 500Å barriers (doped 10^{18} cm^{-3}) of $Al_{0.25}Ga_{0.75}As$. Fifty multiquantum well periods were sandwiched between 1 μm thick (top) and 0.9 μm thick (bottom) layers of doped (10^{18}) GaAs contacts. The number of quantum well periods was reduced to 35 in layer 1289.

The quantum well infrared photodetector is an extrinsic photoconductor. Infrared detection is via intersubband or bound-to-extended state transitions within the multiple quantum well superlattice structure. Due to the polarization selection rules for transitions between the first and second quantum wells, the photon electric field must have a component parallel to the superlattice direction. Light absorption is thus anisotropic with zero absorption at normal incidence. The QWIP detector's spectral response is also narrowband, peaked about the absorption energy. The wavelength of peak response can be adjusted via quantum well parameters and can be made bias dependent.

To maximize the polarization-dependent coupling efficiency, which is designated in this report as C_p, gratings were processed by reactive ion etching to a depth of 0.7 μm into the top contact layer. The gratings have a square profile with 50% duty cycle and 3.2 μm period. The reflective gratings were etched on top of the detectors to disperse the normally incident radiation through the backside of the substrate to give a component of light with electric vector perpendicular to the quantum wells for maximizing optical coupling efficiency. Both mechanical thinning and addition of an AlAs waveguide layer were tested as alternative schemes for increasing optical coupling. The QWIP detector cross section is shown in Fig. 2.

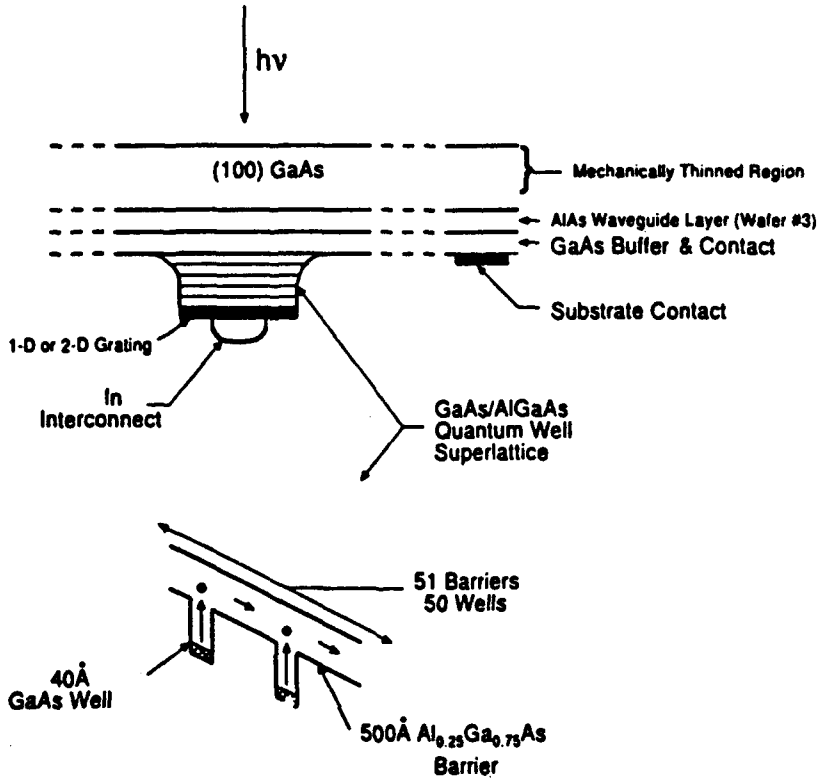

Fig. 2 GaAs/AlGaAs QWIP detector cross section.

The first QWIP layers (e.g., 1047 and 1195) used one-dimensional (1-D) lamellar gratings with a grating constant of 3.5 μm. In subsequent wafers, two-dimensional (2-D) square gratings with a grating constant of 3.0 μm were used (e.g., 1242). In both types of gratings, the grating height was 0.7 μm. To further improve optical coupling and reduce crosstalk, additional coupling-improvement techniques undertaken included adding an AlAs layer on additional wafers (1285, 1286 and 1289) to create a resonant optical cavity. In addition, several hybrid FPAs were mechanically thinned using a diamond mill.

The evolutionary improvements applied to the successive QWIP wafers produced an order of magnitude increase in responsivity due to the concomitant improvement in optical coupling. To discriminate between possible increase in absorption quantum efficiency and the improvements in polarization dependent coupling that were achieved, we introduce an effective quantum efficiency, ηC_p, defined as the product of the absorption quantum efficiency, and the polarization dependent

coupling efficiency, ηC_p. The measured ηC_p's reported here are based on the full pixel area rather than the mesa area since scattering off the mesa walls strongly influences the absorption.

2.1 Layer 1195

Measurements of discrete QWIP (n-type AlGaAs/GaAs multiple quantum well infrared photodetectors) test detectors from the initial AT&T detector delivery on this program, designated layer 1195, are reported in this section; hybrid FPA test data using arrays from this layer is reported elsewhere. The detector's current-voltage (I-V) characteristics, noise power spectra, and responsivities were evaluated on a limited number of elements. Measurements were performed as a function of temperature and bias voltage under both high (approximate f/# = 0.5) and low (essentially zero field of view) infrared background conditions. Since detector response to input infrared radiation is linear, detector performance figures of merit may be determined for all infrared backgrounds and detector temperatures from this data. We extract corresponding detector D* values.

The detectors were fabricated in a standard QWIP wafer. Standard is defined in Fig. 3 of AT&T's Quarterly Progress Report for this program dated April 1992. We have included this figure as Fig. 3 in this report for ease of reference. The peak response wavelength is 8.8 microns, and a nominal 50% response long wavelength cutoff of 9.5 microns. The detectors do not exhibit broadband response at short wavelength (i.e., the response is peaked). Detector spectral response exhibits some nonuniformity that may be related to the difficulty of matching grating peak response with detector spectral response. QWIP spectral response characteristics are not strongly dependent on either bias voltage (within a range of ± 5 volts) or temperature (less than 100K). Linear gratings were etched into the top side of the mesas which define these detectors to enhance response to backside normal incidence illumination. The QWIPs evaluated were 200 μm square or 200 μm diameter circular detectors. No substantive difference was observed between these two geometries that could not be accounted for by the area difference.

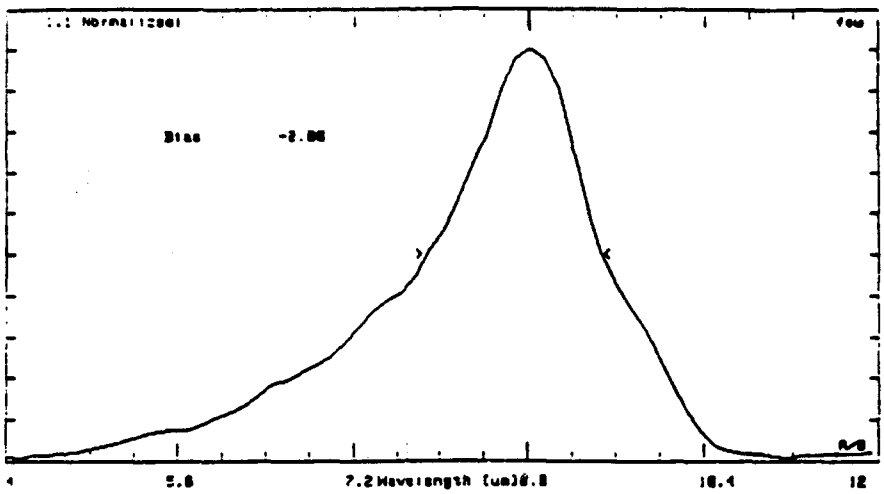

Fig. 3 Spectral Response for Layer 1195.

2.1.1 Low Background Measurements

Measurements of detector dark current and noise were performed under zero field of view conditions to characterize detector properties without having to contend with infrared radiation induced photocurrents. The detector dark current mechanisms revealed by these measurements limit minimum achievable detector noise as a function of temperature and bias voltage. The infrared background was low enough that no significant photocurrent was introduced, relative to the measured dark current, at any temperature.

The detector I-V characteristics exhibited excellent uniformity. A cumulative distribution function of the measured R_0A products at 78K is shown in Fig. 4. At this temperature, current is limited by thermionic emission of carriers from the wells. For the 18 elements sampled, the ratio of the standard deviation to the mean is 4%, demonstrating very good uniformity. The mean R_0A product is 1100 Ω-cm^2. Examination of the I-V characteristics shows that the uniformity of detector characteristics extends beyond uniformity of the inverse of the slope of the I-V characteristic at zero bias. Figure 5 shows the I-V characteristics on linear scales of three detectors at 78K; the curves are extremely close at all bias voltages. The I-V curves in Fig. 5 also demonstrate superlinearity of current with applied voltage, indicating that more carriers are available for conduction with increasing voltage. This behavior is qualitatively consistent with thermionic assisted tunneling and barrier lowering phenomena that are operative in these devices.

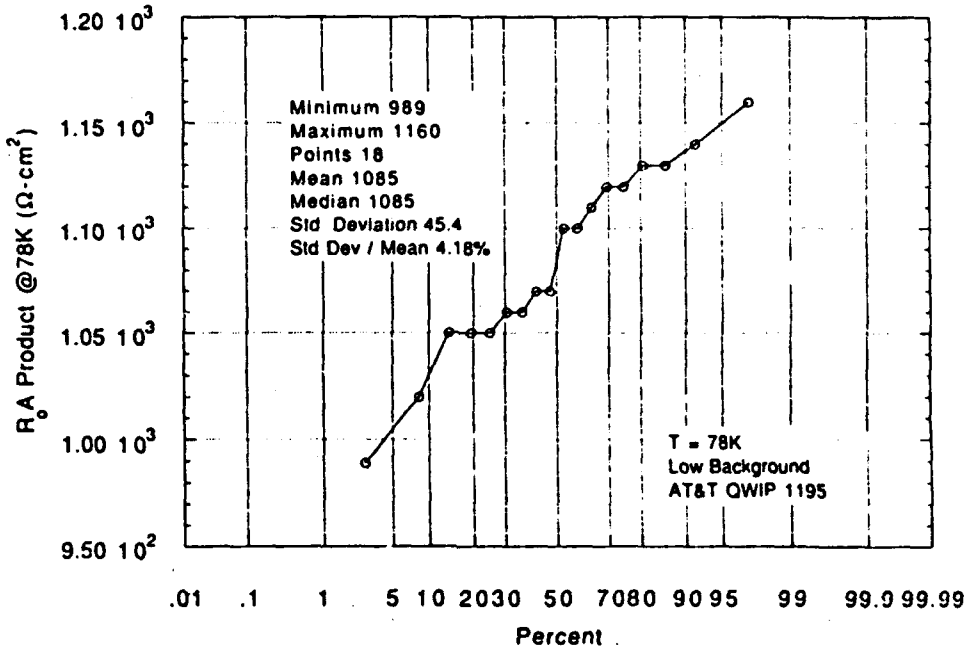

Fig. 4 Cumulative distribution function of R_oA products at 78K for layer 1195.

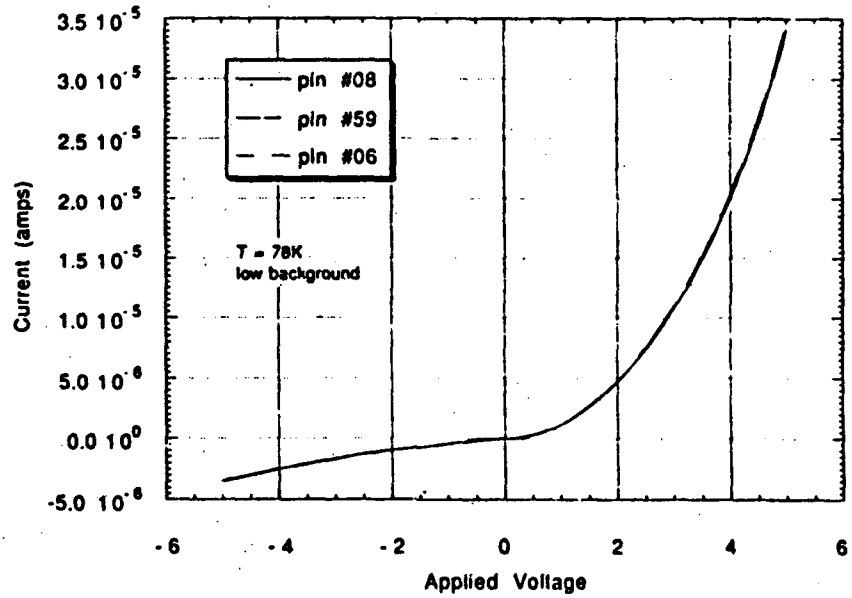

Fig. 5 I-V characteristics on linear scales of three detectors at 78K; the curves are extremely close at all bias voltages.

I-V characteristics vs. temperature over a range from 100K to 11K are shown in Fig. 6. Two detector I-V characteristics are shown in the figure; the curves exhibit that uniformity of performance is maintained to low temperatures. This is important because nonuniform currents associated with imperfections are often revealed especially at low temperatures. The curves indicate that the operative dark current mechanisms are thermionic emission current at low bias voltages, and field emission tunneling current at high bias voltages. No evidence of excess tunnel current was observed down to 10^{-13} amps, the effective system limit for these measurements. This represents a substantial improvement (at least two orders of magnitude reduction) over previously measured detectors of similar design.

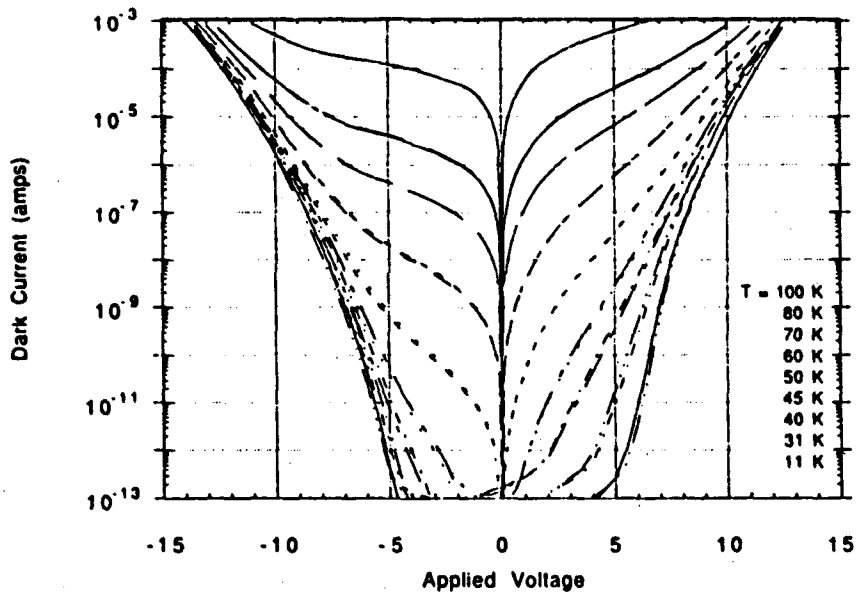

Fig. 6 I-V characteristics vs. temperature from 100K to 11K.

The thermally activated nature of the currents at low bias are shown in Fig. 7, where the log of the dark current at selected bias voltages is plotted vs. inverse temperature. At high bias and low temperature the current is temperature independent, which is characteristic of tunneling mechanisms. The activation energies for the thermionic emission current are determined from the slopes of the curves at high temperature. These activation energies are well-defined, and are shown to decrease with increasing bias voltage.

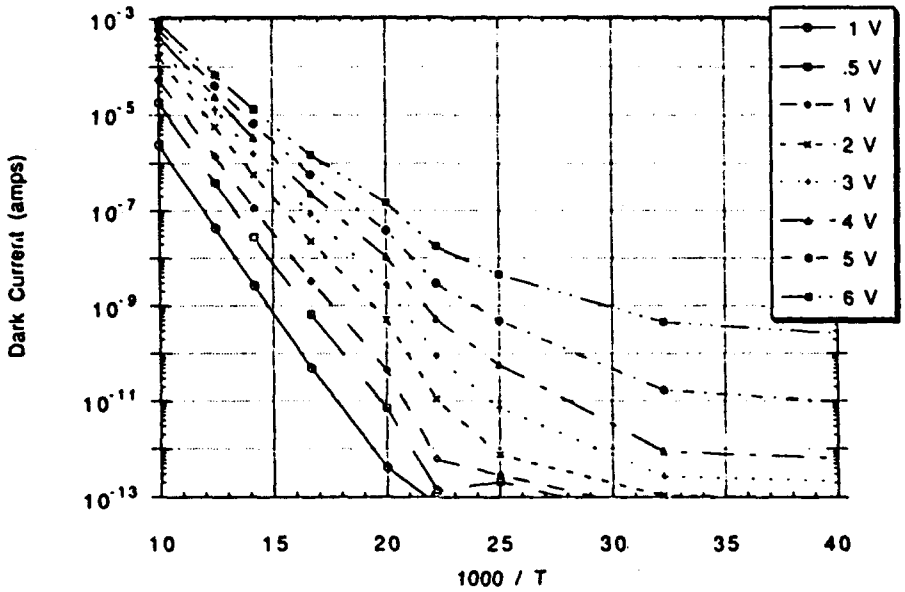

Fig. 7 Layer 1195 dark current at selected bias voltages vs. inverse temperature.

Activation energy data extracted from forward (positive with respect to substrate) and negative bias voltages are shown in Fig. 8. The data show that the activation energy for dark current decreases more rapidly for positive bias than negative bias, and is of course consistent with the larger currents observed under positive bias. The experimentally observed trend is more bias dependent than a Schottky barrier lowering model predicts. At small bias, the activation energy is 141 meV, which is very close to the optical transition energy corresponding to the peak infrared response wavelength of 8.8 microns (141 meV). The Fermi energy is 13.4 meV at 78K, based on the nominal well doping of 1×10^{18} cm^{-3}. Subtracting the Fermi energy from the zero bias electrical activation energy yields an energy corresponding to a wavelength of 9.7 microns; this is also in reasonable agreement with the measured detector cutoff wavelength of 9.5 microns. However, the changes in electrical activation energy with bias are not reflected in changes in detector spectral response with bias, since spectral response is relatively bias independent. This may be a reflection of the fact that phonons are important in the transitions related to dark current, but not for photocurrent.

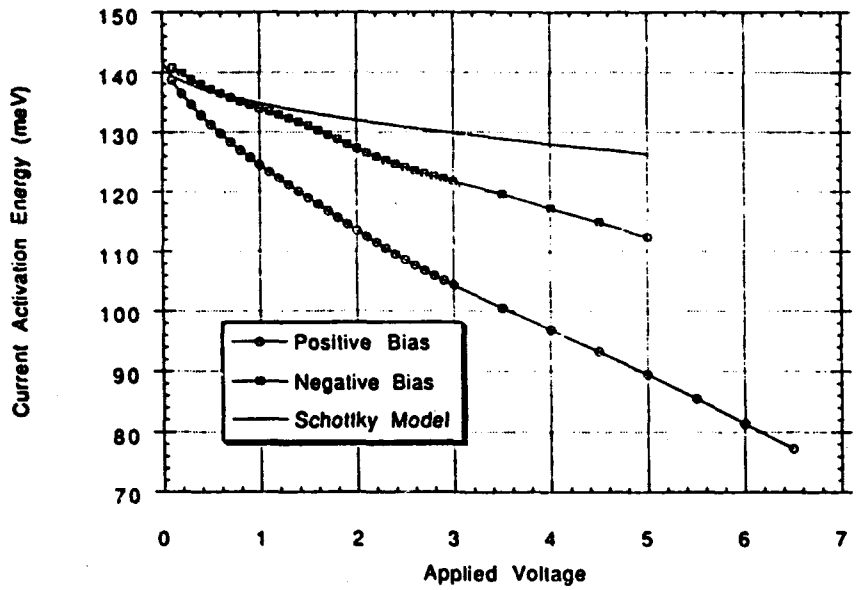

Fig. 8 Layer 1195 activation energy data extracted from forward (positive with respect to substrate) and negative bias voltages.

Noise measurements were performed as a function of bias and temperature; typical results are shown in Fig. 9. The measured white noise current as a function of bias voltage is shown for two detectors at 78K, again demonstrating excellent uniformity; and one of the detectors at 60K. At low enough temperature, detector noise is well below the amplifier noise floor of about 2×10^{-15} amps/Hz$^{0.5}$. The magnitude of the noise current can be interpreted in terms of standard expressions for g-r noise in extrinsic photoconductors.

The decrease in noise at low temperatures is accounted for by decrease in dark current. This is demonstrated in Fig. 10, which shows that the photoconductive gain (transit time / lifetime) derived from these measurements is temperature independent. The photoconductive gain saturates at a value of 0.2 to 0.3 for bias voltage magnitudes in the 2 to 5 volt range. Note that the gain is independent of the polarity of the bias voltage. The increase in gain with applied bias at low voltages and saturation at large bias is typical of photoconductive device operation. Because the QWIP is an extrinsic photoconductor, the saturation in gain is more likely a result of mobility saturation at high electric fields than sweepout effects. Assuming a saturated drift velocity of 10^7 cm/sec, the carrier lifetime is 8×10^{-12} sec. The value of the photoconductive gain is important in relating measured responsivity to effective quantum efficiency.

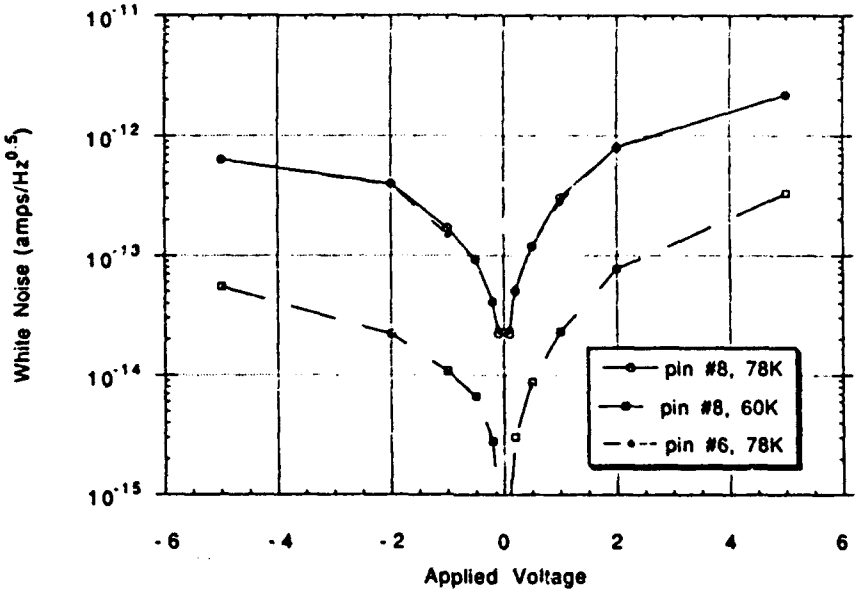

Fig. 9 Layer 1195 noise as a function of bias and temperature.

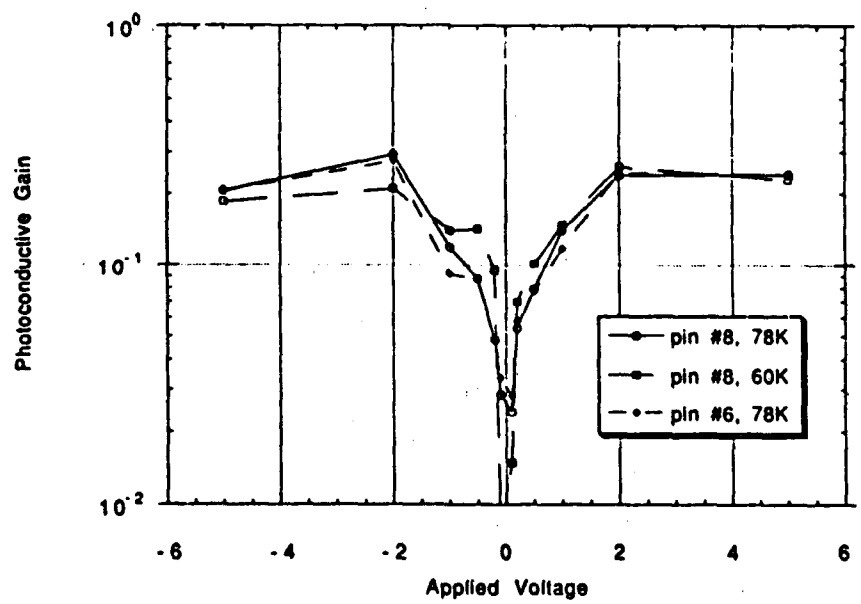

Fig. 10 Layer 1195 photoconductive gain.

2.1.2 High Background Measurements

I-V curves as a function of temperature under high infrared background (wide field of view) are shown in Fig. 11. At low temperature and bias, photocurrent is the dominant current mechanism. The photocurrent is independent of temperature and bias voltage in the 2 to 5 volt temperature range. These observations are consistent with the independence of detector spectral response and saturated photoconductive gain on temperature and bias voltage. Note that the photocurrent is relatively symmetric in bias voltage; this is consistent with the symmetry observed in the photoconductive gain and is not like the asymmetry observed in dark current. For negative bias voltages, thermionic emission dark current is larger than photocurrent for temperatures greater than 60K; for positive bias voltages, dark current exceeds photocurrent at even lower temperatures. Therefore, BLIP detector operation under wide field-of-view conditions dictates operating temperatures less than about 60K for these detectors. The asymmetry in dark current implies improved performance in non-BLIP conditions for negative bias polarities on the detector compared to positive bias polarities.

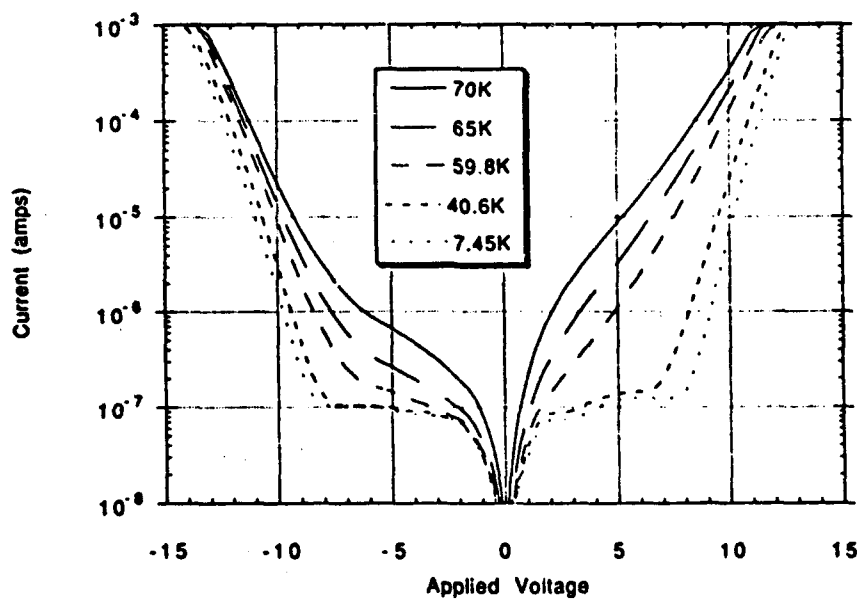

Fig. 11 Layer 1195 detector I-V's under high background.

Noise measurements under high background conditions could be extended to lower temperatures than possible in the case of the dark current measurements without encountering

system limitations. Measurements over the temperature range 60K to 7K are shown in Fig. 12. The noise is temperature independent, as is the detector photocurrent. Photoconductive gain determined from this data and the measured photocurrent are shown in Fig. 13. The photoconductive gain values at 60K are in reasonable agreement with those obtained from the dark current measurements, although slightly higher values are indicated at the lowest temperature. This data indicates that noise is simply related to total current, irrespective of the nature of its origin (dark current or photocurrent).

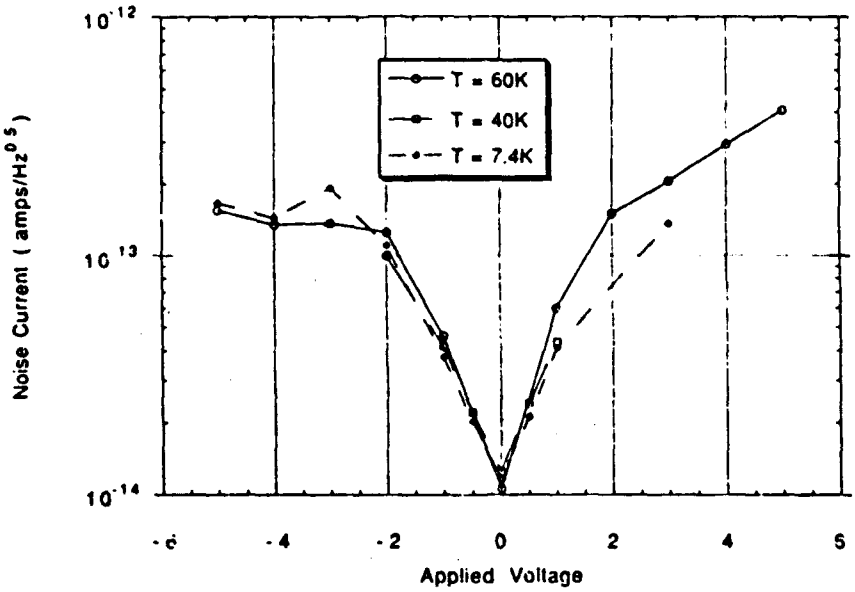

Fig. 12 Layer 1195 detector noise vs. temperature under high background.

Responsivity measurements were performed using an f/2 lens to focus modulated blackbody radiation into the detector optically active area. Typical results are shown in Fig. 14 for a detector measured at two temperatures. The responsivity increases with bias and saturates in the 2 to 5 volt bias range. The symmetry, lack of temperature dependence, and bias dependence are consistent with the photocurrent and photoconductive gain measurements. The magnitude of the responsivity is in the 20 to 30 mA/watt range for bias voltages greater than 2 volts. Using the photoconductive gain determined from noise measurements (0.3), the responsivity is consistent with an effective quantum efficiency of 1%. These results are four times lower than the values obtained on detectors measured in an FPA configuration (see hybrid test data). The hybrid data, however, is taken under flood illumination conditions; the difference is that radiation is incident

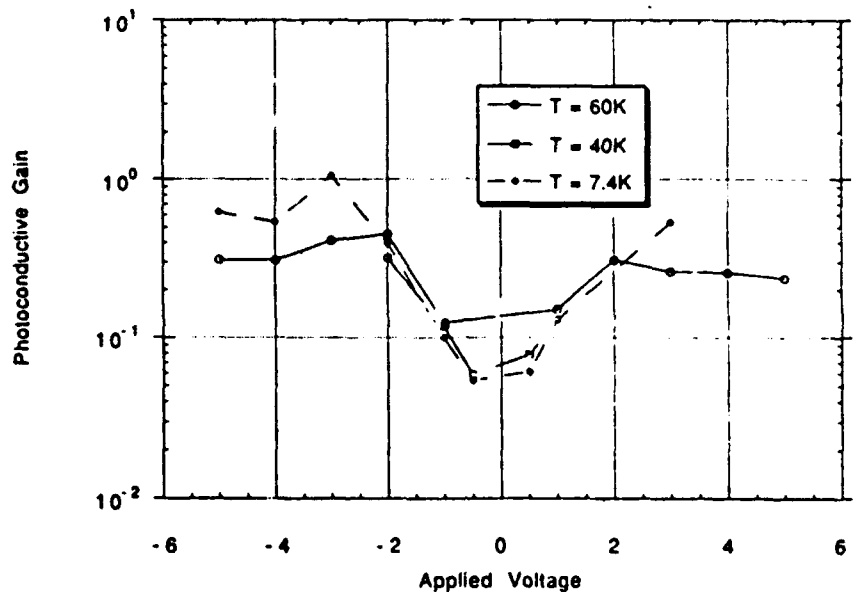

Fig. 13 Layer 1195 photoconductive gain vs. temperature under high background.

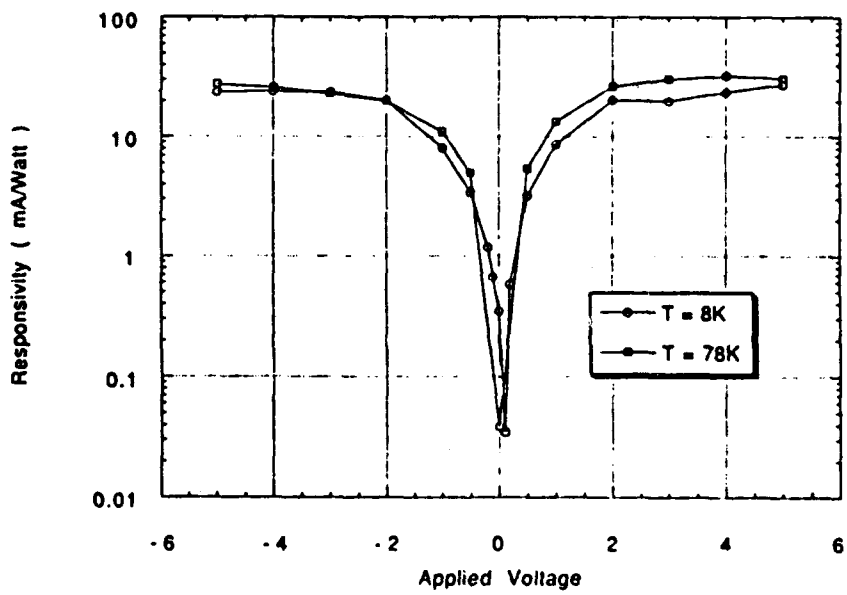

Fig. 14 Layer 1195 Responsivity vs. Bias at 8K and 78K.

over the entire array of detectors. The flood illumination measurement technique is more susceptible to scattered light effects, which can result in light that not directly incident on the detector contributing extra detector photocurrent. For comparison, flood illumination measurements were also performed on the test detectors; and resulted in 6% quantum efficiency on the same test detectors, which gave 1% quantum efficiency using the focused spot technique. Additional work subsequently resolved the substantial discrepancy in responsivity values obtained by these two techniques as simply crosstalk in the unthinned substrates. The high crosstalk was ultimately eliminated by mechanically thinning the substrates to ≈30 μm.

The detector optically active area may be determined by measuring the increase in signal resulting from increasing the limiting aperture size at the blackbody. As long as the imaged aperture is smaller than the detector, detector signal increases linearly with aperture area. When the imaged aperture is larger than the detector, the detector signal reaches a constant that is proportional to the detector quantum efficiency–active area product. This product is relevant to the responsivity and responsivity uniformity in an array. An example of such a measurement is shown in Fig. 15. Analysis of the data in the figure results in an integrated optically active area of 5×10^{-4} cm^2. This number is in reasonable agreement with the physical size of the detector (200 microns square) and the measured distance between 50% response point (FWHM) of 205 microns. The measured quantum efficiency active area product on eleven 200 micron square detectors is shown in Fig. 16 at ± 2 volts. The ratio of the standard deviation to the mean value is 4% at -2 volts, and better uniformity was achieved for negative bias voltages.

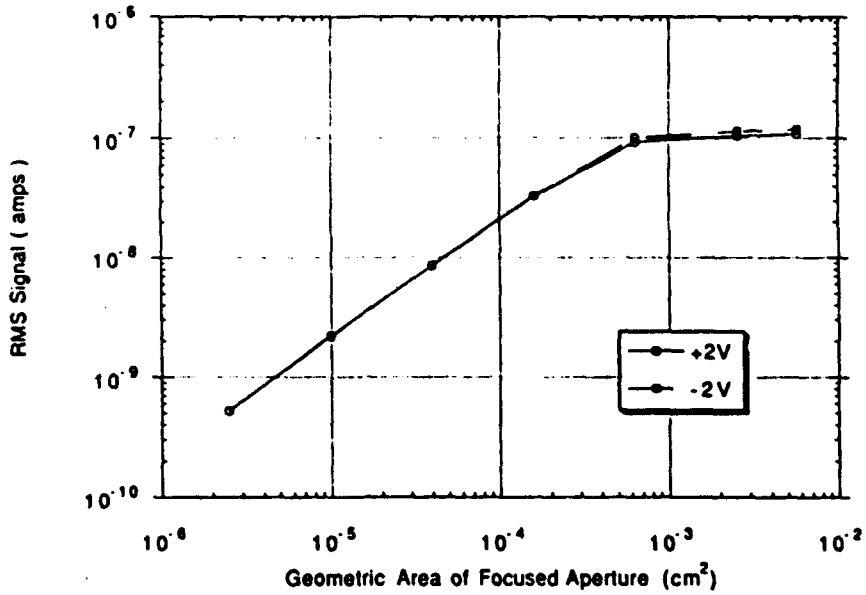

Fig. 15 Layer 1195: Determination of optically active area.

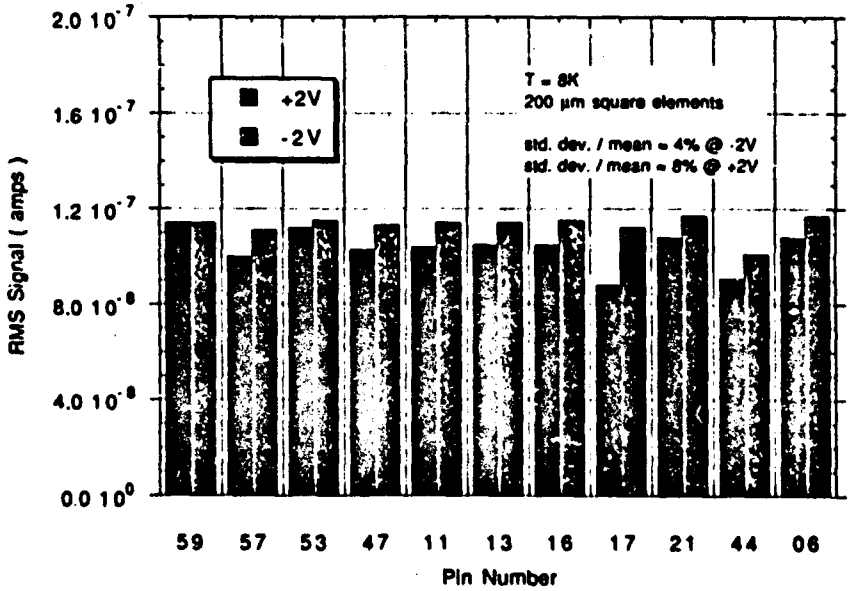

Fig. 16 Quantum efficiency active area product for 11 detectors.

2.1.3 Summary

Characterization of the first set of n-type AlGaAs/GaAs QWIP test structures using a linear grating for responsivity enhancement showed similar performance at higher temperatures to that obtained from devices delivered by AT&T a year earlier. Somewhat lower thermionic emission current and reduced responsivity were observed on the new devices. The reductions may have resulted from a decrease in carrier density in the wells, which is difficult to evaluate by independent means. Accurate responsivity measurements are complicated because of scattered light and crosstalk from the gratings and mesa edges, and require further investigation.

The most distinguishing feature of the Layer 1195 devices is the absence of evidence of excess tunnel current, which is important for achieving high detectivity at low backgrounds and temperatures. The devices are limited by thermionic emission currents at operating bias voltages consistent with detector operation, and noise mechanisms are well described g-r expressions for extrinsic photoconductors. The detector limited D* of these devices is 3.5×10^9 cm-Hz$^{0.5}$/W at 80K and 9.5×10^{12} cm-Hz$^{0.5}$/W at 45K. These values are obtained from detector measurements at -2 volt bias, and reflect a responsivity of 20 mA/watt and a photoconductive gain of 0.3. A plot of the detector limited D* values vs. temperature is shown in Fig. 17. For wide field of view, the detectors are BLIP limited below 60K. The uniformity of the devices is excellent; standard deviation to mean ratios of 4% were obtained for both dark current and responsivity.

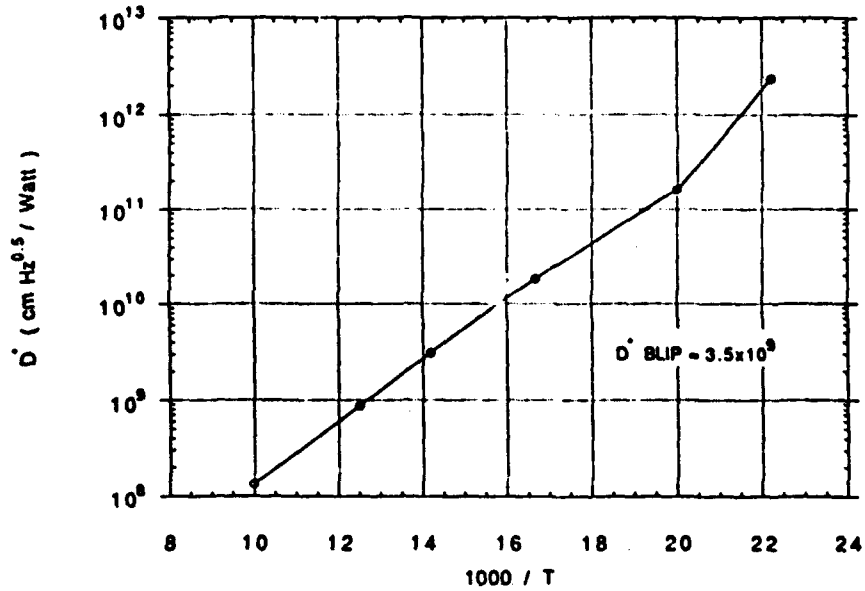

Fig. 17 Layer 1195 detector-limited D* vs. reciprocal temperature.

2.2 Impact of Optical Coupling Improvements on Discrete Detector Performance.

Characterization of test detectors from four AlGaAs/GaAs quantum well infrared photodetector (QWIP) wafers generally showed agreement between the measurements performed at AT&T and ' ;e performed the same way at Rockwell. A summary of the performance obtained on these wafers at Rockwell is shown in Table 2. Wafer 1047 and 1195 use 1-dimensional stripe gratings to provide response at normal incidence, wafer 1242 uses a 2-dimensional square grating, and wafer 1289 uses both a 2-dimensional grating and an AlAs waveguide. The quantum well architecture is nominally the same for all four wafers, except that wafer 1289 has 35 quantum wells instead of 50 wells as for the other three.

Responsivity is a key performance parameter for any infrared detector. For the QWIP detectors compared here, the responsivity is highest on wafer 1289, at 376 mA/Watt and -2 volts bias. All responsivity measurements in Table 2 were obtained by focused spot measurements, a point to be explained subsequently. Most of the improvement compared to the other samples is attributed to the waveguide and 2-dimensional grating; but note from Table 2 that samples with higher thermionic emission current, as measured by the current density at -2 volts bias, also have

higher responsivity. This indicates that factors other than optical design also contribute to response improvement, such as variation in well doping or carrier mobility. The current-voltage (I-V) characteristics of representative elements from the four wafers measured at 78K under zero field of view conditions are shown in Fig. 18 for comparison. Note also that there are differences in the shape of the I-V characteristics for these samples, indicative of slight structural or transport related variations from sample to sample. These are genuine sample differences, since the I-V characteristics of different devices in a given wafer are quite well matched. The increase in tunneling current at large bias for sample 1289 is consistent with the reduced number of quantum wells in that sample, which leads to larger electric fields at the same applied bias compared to the other samples.

Table 2

Comparison of QWIP Discrete Detector Performance

Layer Number	1047	1195	1242	1289
Type	1D Grating	1D Grating	2D Grating	2D Grating & Waveguide
J @ -2V, 78K (A/cm^2)	3.95×10^{-3}	2.15×10^{-3}	4.98×10^{-3}	1.24×10^{-2}
Peak Responsivity (A/W)	0.040	0.020	0.043	0.376
Peak Wavelength (μm)	8.8	8.8	8.8	9.6
PC Gain @ -2V (V/V)	0.46	0.37	0.35	0.77
ηC_p (Effective QE)	1.2%	0.77%	1.7%	6.3%
D* @ -2V, 78K ($cm\text{-}Hz^{1/2}/W$)	1.2×10^9	9.0×10^8	1.3×10^9	4.8×10^9

Noise characteristics are a second key detector performance parameter. Measurement of white noise was used to obtain the photoconductive (PC) gain for detectors from all four wafers. The PC gain values at -2 volts are shown in Table 2. Values of 0.4 to 0.5 are typical, with somewhat higher values reported for sample 1289. Some increase in PC gain is expected, since it has fewer quantum wells. A PC gain of 0.5 results in noise spectral density in agreement with shot noise calculations. From the responsivity and PC gain values, effective quantum efficiency can be determined, and is reported as QE * Cp (quantum efficiency coupling coefficient product) in Table 2. Detectors in wafer 1289 absorb 6.3% of the incident radiation, while previous wafers absorb 1% to 2%. Zero field of view D* measured at -2 volts at 78K is shown for these detectors

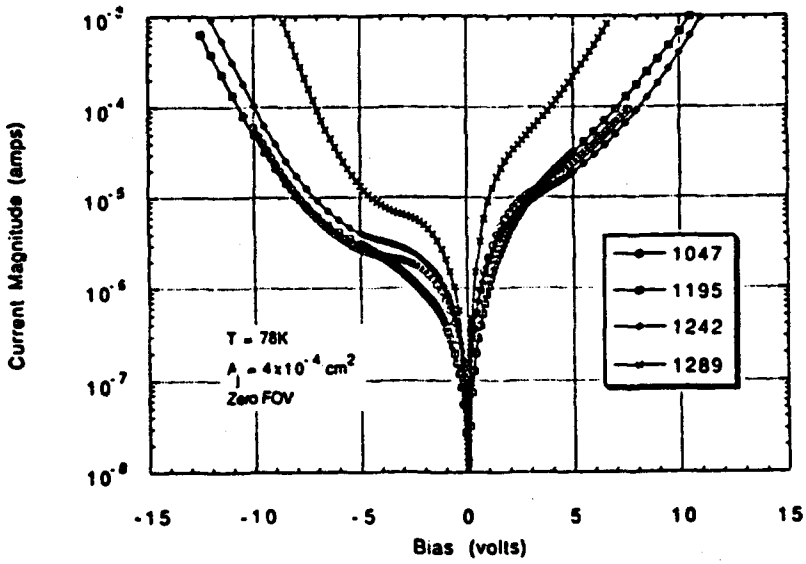

Fig. 18 Comparison of 78K I-V characteristics for four wafer samples.

in Table 2; the best result is 5 x 10^9 cmHz$^{1/2}$/Watt for wafer 1289, which is well below BLIP limits even for wide detector field of view.

We mentioned that the responsivity measurements were made by a focused spot technique. This is important because flood measurements overestimate responsivity by a large factor, due to optical crosstalk. The focused spot measurement system schematic is shown in Fig. 19. With this system, all incident radiation is focused within a single detector; the lens area and distance from the blackbody source determine the amount of radiation incident on the detector. A summary of responsivity measurements obtained with this system is shown in Fig. 20; the responsivity is a factor of 3 to 6 less than that obtained from flood measurement data. The flood technique, which is most typically used for detector evaluation, does not use a lens, but instead uses the detector area and detector to source distance in the radiometric calculations. The problem with the flood technique is that illumination of the entire array can scatter light to the sampled pixel, so that extra signal is derived from reflections of the source in auxiliary structure.

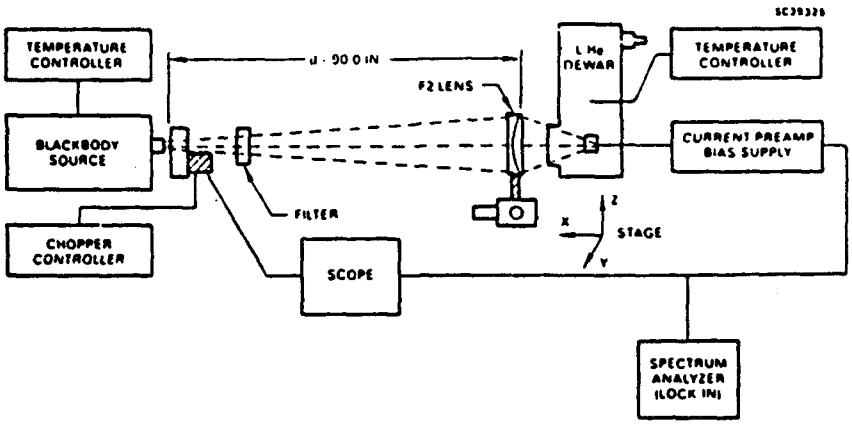

Fig. 19 Focused spot measurement system.

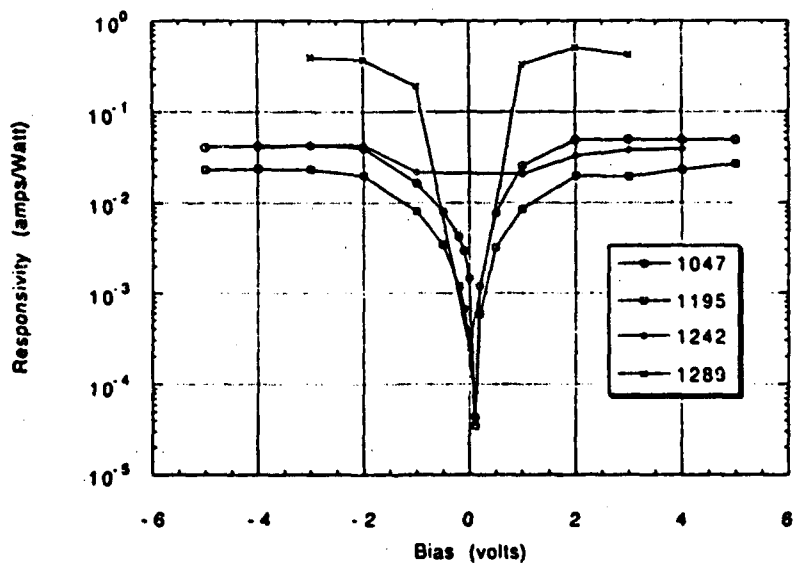

Fig. 20 Comparison of responsivity measurements.

We verified that optical crosstalk is responsible for the large difference obtained by the two techniques by making focused spot measurements on a 128 x 128 focal plane array. As shown in Fig. 21, a portion of the array is illuminated while the total signal induced in all the array elements is monitored. In a sense, this is the inverse of the experiment done on the test detectors in flood illumination mode where a single detector is monitored while the whole array is illuminated. From a comparison of the response obtained within the illuminated region and the total signal from sum

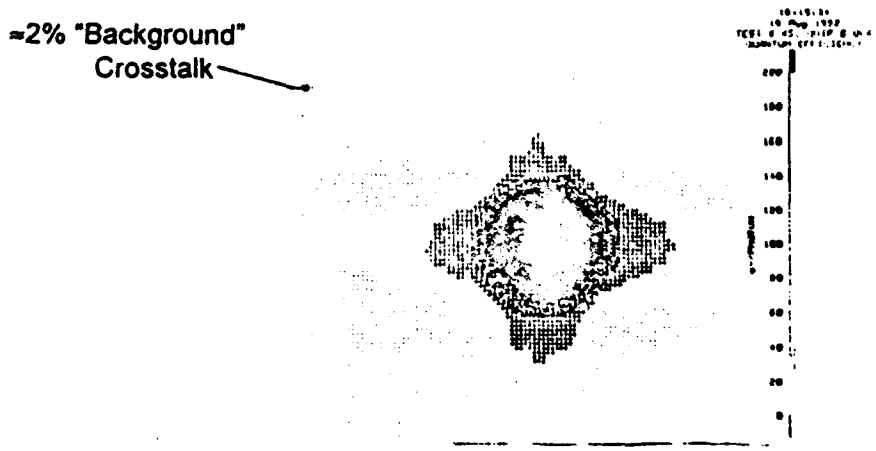

$$\frac{\text{FLOOD}}{\text{SPOT}} = \frac{\text{TOTAL SIGNAL}}{\text{FOCUSED BEAM}} = \frac{11.9\text{mV} \times 15294}{467\text{mV} \times 93.6} = 4.16$$

Fig. 21 Focused spot measurement showing excess signal generated by crosstalk at FPA level.

of the response in all the array elements, the FPA measurement shows a ratio of flood to focused responsivity of 4.2, which is in fair agreement with a factor of six difference obtained on test detectors from this layer. Precise correlation is not expected, since the magnitude of the difference will depend on array configuration, which is different between the test chips and the detectors used in the FPA.

The extra response obtained in the flood mode is not useful for detectors operated in imaging systems, and overestimates detector responsivity. The inflated responsivity values lead to overestimates of quantum efficiency, D* and NEΔT. We note that flood responsivity measurement on layer 1289 gives results in the 1–2 Amps/Watt range, which are among the best values reported in the literature. However, nearly all responsivity measurements reported in the literature are obtained by the flood technique. Having identified this optical crosstalk issue, we can reduce the magnitude by several techniques; such as thinning the substrate, increasing detector fill factor, antireflection coating the substrate, and/or incorporating microlenses. In practice, thinning the substrate effectively eliminated the crosstalk, and no further improvement was necessary.

BLIP detectivities were not obtained at 78K. This is clearly demonstrated in Fig. 22, where we have displayed the current-voltage characteristics of a device from layer 1289 under zero field of view conditions at 78K and wide field of view (approximately f/1) at low temperature. The 78K I-V characteristic is a measure of thermionically emitted dark current and low and moderate bias, and has a thermally activated temperature dependence. The low temperature characteristic is entirely dominated by photocurrent, and is nominally temperature independent. The dark current at 78K is 1.5 orders of magnitude higher than the photocurrent, indicating that detector operation at 78K will be difficult; BLIP operation is achieved only below about 60K.

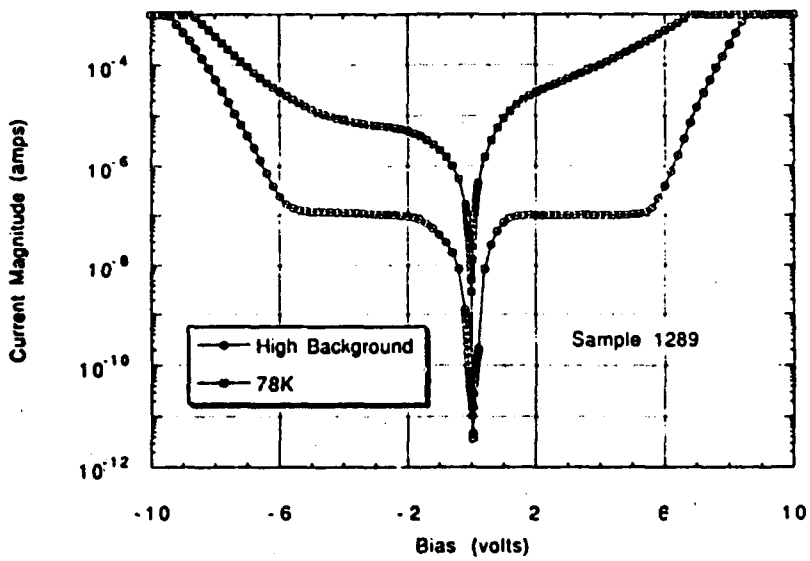

Fig. 22 Comparison of high temperature dark current and high background photocurrent.

Because the thermionic emission current continuously drops as the temperature is lowered, high BLIP limited D* can be achieved at low temperature under low background conditions. This is demonstrated in Fig. 23, which shows detector limited (zero field of view) D* at -2 volts determined from temperature dependent I-V characteristics. A D* of 2 x 10^{12} cmHz$^{1/2}$/Watt is obtained at 45K. At lower temperatures, measurement system limitations made accurate current measurements impossible; but, measurements on QWIP FPAs have shown this trend to continue to even lower temperatures. Hence, these detectors are attractive for use at low temperatures in low infrared background conditions, where HgCdTe detectors suffer from large detector nonuniformities associated with dark current variations

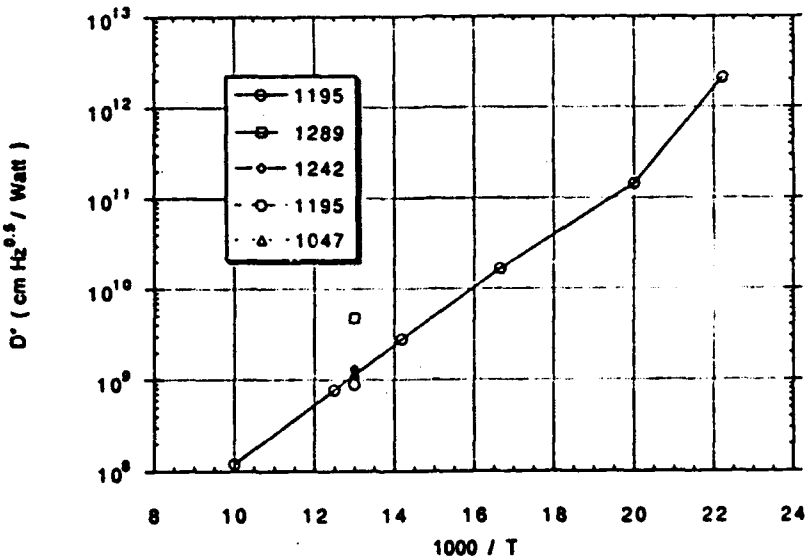

Fig. 23 Zero field-of-view D* vs. Temperature.

2.3 Summary of Layer 1285 and Layer 1286 Detectors

We also evaluated test detectors from AT&T layers 1285 and 1286 in great detail. I-V curves, responsivity, spectral response and noise data were collected. These resulted are summarized and compared with Layer 1289 in Table 3. In the case of Layer 1285, R_0A at 78K exhibited mean value of ≈6000 with larger variation than previously observed; the peak wavelength was typically ≈9 microns; and responsivity was ≈140 mA/watt (2% QE) at -2V and 78K. A slight decrease in responsivity was observed at lower (6K) temperature. The photoconductive gain was 0.36 @ -2V and 0.74 @ -3V at 7.4K.

For layer 1286, the R_0A at 78K was roughly 7000 with similar variation as 1285, peak wavelength was approximately 9 μm, and the responsivity was ≈140 mA/watt (corresponding to an ηC_p of 2%) at -2V and 78K. Again a slight decrease in responsivity was observed at lower (6K) temperature. The photoconductive gain for two different devices was 0.39 and 1.13 for at -2V and 7.4K. Excess noise was observed in many devices, particularly for forward bias conditions.

Table 3

Comparison of Layers 1285, 1286, and 1289

Layer Number	1285	1286	1289
Type	1D Grating	2D Grating	2D Grating & Waveguide
R_oA (A/cm^2)	6000	7000	700-1000
Peak Responsivity (A/W, focused spot)	0.144	0.150	0.376
Peak Wavelength (μm)	≈9	9.2	9.6
PC Gain @ -2V (V/V)	0.36 (0.74 @-3V)	0.39 (1.13 @ -3V)	0.77
ηC_p (Effective QE)	2%	1.7%	6.3%
D* @ -2V, 78K (cm-$Hz^{1/2}$/W; focused spot)	1.79×10^9	1.8×10^9	4.8×10^9

3.0 CMOS Readouts

We fabricated hybrid 128 × 128 FPAs by mating the QWIP detector arrays supplied by AT&T Bell Laboratories to either of three CMOS readout multiplexers via indium interconnects. The three CMOS readouts[25] have direct injection,[26] gate modulation[27] or electronically scanned buffered direct injection[28] input circuits. The direct injection circuits were used for high background tests including conventional imaging. Gate modulation was used for low background characterization since it has self-adjusting current gain for attaining low read noise at low background as long as the detector current is dominated by the photocurrent; i.e., the detectors have low dark current. FPA data implies QWIP detector dark current of ≤ 0.3 fA at 2V bias and 40K operating temperature for material having ~ 8.7 μm peak wavelength.

3.1 High Capacity Direct Injection Readout

The 128 x 128 high capacity direct injection (HCDI) readout is a CMOS readout designed for high background applications. It was originally developed in 1988 using a custom 2 μm process (two-metal, single-poly) at Orbit Semiconductor on the same 4" wafer as the other 128 x 128 readouts. Die size is about 1.15 x 0.9 cm^2.

The HCDI readout has a high uniformity direct injection input and large charge handling capacity that, at the time of development, represented a significant enhancement in the state of the art. The maximum charge capacity is typically > 9.25 x 10^7 carriers at 5V operating voltage. Input offset nonuniformity is also consistent with the state of the art with total peak-to-peak variation across a die of typically < 3 mV pk-pk. The readout has a CMOS switched-FET architecture having maximum 5 MHz data rate capability at 12-bit signal fidelity. Figure 24 shows a condensed schematic. The unit cell size is 60 x 60 μm^2.

The unit cell layout maximizes integration capacitor area within the constraints of the 2 μm process. The as-drawn capacitor uses 75% of the available area and has estimated value of 3.6 pF using 250Å thermal oxide. The measured charge-handling capacity is in good agreement with that predicted for the 5V supply voltage. The large charge-handling capacity allows sub-10 mK NEΔT and full-frame imaging at 60 Hz with a variety of detector material systems.

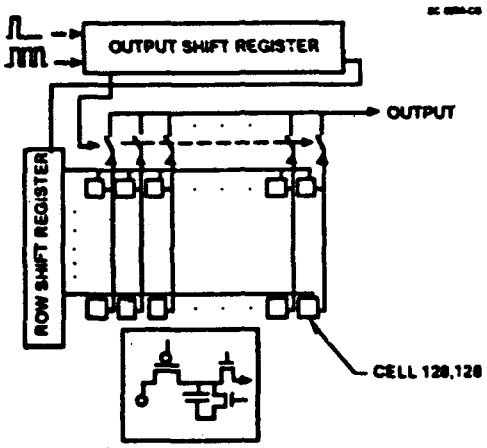

Fig. 24 128 x 128 High Capacity Direct Injection Readout.

The device can be operated using simple support electronics. The user-friendly interface translates to reduced IR sensor complexity for rapid insertion into IR systems. There is no need to develop elaborate support chips for either operation or interface. The device can operate using only three CMOS clocks (0 to 5 or 6V), two fixed dc voltages and one variable voltage to optimize the detector bias. Table 4 lists the readout high capacity direct injection readout characteristics. This readout was the workhorse for the program.

Table 4

High Capacity Direct Injection Readout Characteristics

Parameter	Nominal	Maximum	Units
Format	128 × 128		Pixels
Cell Size	60 × 60		μm^2
Input Circuit	Direct Injection		
Output Amplifier	Source Follower		
Package	68 pin LCC		
Clocks	3	4	
DC Supplies	1	4	
Built-in Test Points	3		
Charge Capacity	74	92.5	10^6 e-
Read Noise (typ.)	<500	<1000	e-
Frame Rate	60	>200	Hz
Maximum Dynamic Range	$>10^5$		dB
Pixel Data Rate	1	5	MHz
Input Offset Nonuniformity	3		mV p-p
Readout Transfer Ratio	27.0		nV/e-

3.2 Gate Modulation Readout

The primary 128 x 128 readout used for QWIP FPA evaluation at low backgrounds has gate modulation input with p-MOSFET load (Fig. 25). Detector current, including photocurrent and dark current, flows through the load device while a proportional current flows into the integration capacitor via a p-MOSFET input FET (20 μm width and 10 μm length). The gain and dc level are adjusted by varying the source voltage (GMODS) of the input FET (6 μm width and 49 μm length). Cell access, cell reset, and video multiplexing are performed by enabling and disabling switch-FETs via static CMOS shift registers. The switched-FET readout has a single output with minimum slew rate of 3.9 V/μsec and maximum output excursion of ≤ 2 V. Maximum power dissipation is 8.4 mW.

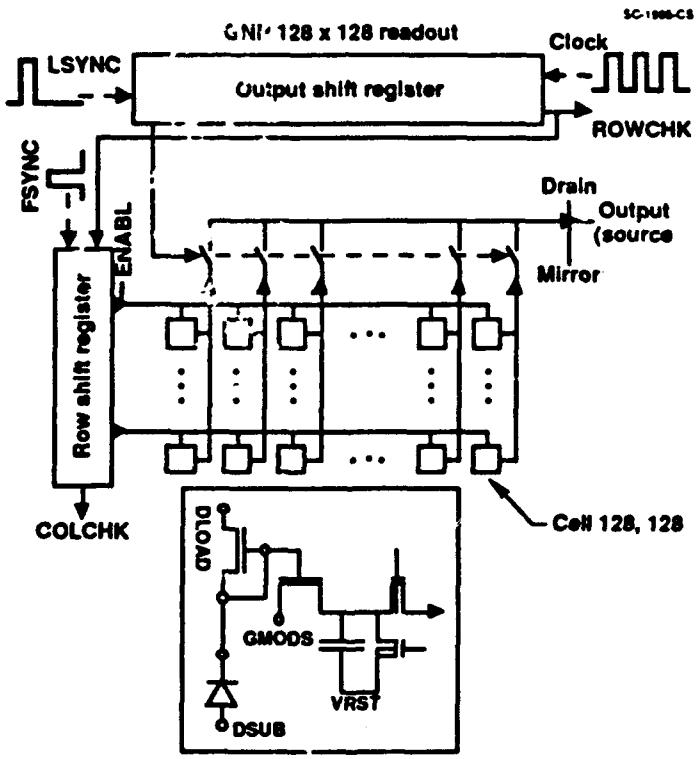

Fig. 25 128 x 128 Readout With Gate Modulation Input and CMOS Switched-FET Readout Architecture.

The 128 x 128 readout was fabricated using a custom 2 μm CMOS process at Orbit Semiconductor. Good fabrication yield was achieved, but p-MOSFET characteristics were peculiar

due to the presence of a parasitic edge transistor. The main impact of the short-channel edge transistor on FPA performance was increased, but manageable, 1/f noise at operating temperatures < 100K.

Gate Modulation Current Gain. The current gain of the gate modulation input circuit is approximately:

$$A_I = \frac{g_m}{g_{m,LOAD}} \eta_{inj}; \quad \eta_{inj} = \frac{g_{m,LOAD} R_{det}}{1 + g_{m,LOAD} R_{det}} \left[\frac{1}{1 + \frac{j\omega C_{det} R_{det}}{1 + g_m R_{det}}} \right] \tag{1}$$

where η_{inj} is the injection efficiency of detector current into the load transistor, g_m is the input FET transconductance, $g_{m,LOAD}$ is the load FET transconductance, and C_{det} and R_{det} are the detector resistance and capacitance, respectively.

The signal integrated in the integration capacitor is a dc-suppressed, gain-proportioned facsimile of the total detector current. Any changes in load current modulate the integrated current via the gate of the input FET. For highest current gain and best circuit noise figure, the detector dark current must be small relative to the photocurrent for minimization of load FET thermal noise and maximization of current gain to reduce the impact of input FET thermal noise. The circuit not only is capable of near-zero bias operation via the low threshold nonuniformity achieved, but prefers it since excess detector dark current generates additional detector shot noise and load FET thermal noise.

The operating point is established by concurrently adjusting the detector substrate voltage (DSUB) and the source voltage (DLOAD) of the load MOSFET. The current gain and the integration capacitor percentage fill is then set by either adjusting GMODS, or by equivalently shifting the DLOAD and DSUB biases. Using a laboratory mechanization of this adaptive bias control, minimum total dynamic range of 200 dB has been achieved.

The use of a MOSFET as an active load device provides dynamic range management via automatic gain control in combination with adaptive background pedestal suppression.[29,30] The current gain self-adjusts by orders of magnitude depending on the total detector current. Input-referred read noise of tens of electrons[31] can thus be achieved with high impedance QWIP detectors (at low temperature and background) since the read noise is approximately:

$$N_{read} = \frac{\left(I_{load}^2 + I_{input,ir}^2 + I_{mux,ir}^2\right)^{1/2} t_{int}}{q} \tag{2}$$

where I_{load}^2, which is the composite thermal and 1/f noise of the load device, is

$$I_{load}^2 = \int^{\Delta f} \frac{1}{\eta_{inj}^2}\left(\frac{8}{3}kTg_{m,load\,FET} + \sigma_{load}^2 g_{m,load\,FET}^2\right)df \tag{3}$$

The input FET is often subthreshold; the input-referred input circuit noise, $I_{input,ir}^2$, is consequently

$$I_{input,ir}^2 = \int^{\Delta f}\left[\frac{1}{A_I^2}\left(2qI_{input} + \frac{K_{input\,FET}^2\, g_{m,input\,FET}^2}{f^{\alpha}}\right)\right]df \tag{4}$$

The dominant input-referred readout noise, $I_{mux,ir}^2$, is

$$I_{mux,ir}^2 = \frac{1}{A_I^2}kTC_{input}\Delta f \tag{5}$$

where C_{input} is the total input capacitance including the capacitance of the bus line servicing the entire column.

For the limiting low background case where the current gain is sufficiently high for the load FET noise to dominate the total readout noise and where the photovoltaic detector impedance is satisfactorily high, the minimum read noise is approximately

$$N_{min} \approx \sqrt{\frac{4}{3}\frac{I_{det}t_{int}}{q\eta_{loadFET}}} \tag{6}$$

where $\eta_{load\,FET}$ is the subthreshold ideality of the load MOSFET, I_{det} is the total detector current, and t_{int} is the integration time. The minimum read noise is thus proportional to the photogenerated shot noise (N_{shot}):

$$N_{min} \approx N_{shot}\sqrt{\frac{4}{3}\frac{1}{\eta_{loadFET}}} \tag{7}$$

The circuit's current gain thus compensates at low background to maintain a relatively constant percentage of BLIP if the detectors have satisfactory quality.

Summarized in Table 1 are the readout characteristics. The device offers large total dynamic range in trade for higher gainer uniformity and stricter requirements on MOSFET threshold uniformity and dc bias noise. The minimum instantaneous dynamic range is typically > 65 dB, while the overall dynamic range can be > 140 dB using adaptive bias adjustment.

Table 5
Gate Modulation 128 x 128 Multiplexer Characteristics

Parameter	Value	Units
Nominal Supply Voltage	6	V
Maximum Charge Capacity	61	10^6 e-
Total Dynamic Range	>1	10^5
Minimum Instantaneous DR	>1	10^3
Total Dynamic Range (Adaptive)	>1	10^7
Responsivity Nonuniformity	3:1	Max:Min
Maximum Data Rate	≥4	MHz
Input Offset Nonuniformity	<4	mV p-p
Transfer Ratio	29.6	nV/e-

3.3 Electronically Scanned Buffered Direct Injection Readout

One of the QWIP arrays from layer 1286 were hybridized to a 128 x 128 readout having electronically scanned architecture with buffered direct injection input.[32] The readout offers a combination of features in the 60 μm pitch, which at the time of development were unique. These include high charge capacity, low input impedance (for efficient interface to detectors with R_0A product significantly lower than Ω-cm^2), low input offset nonuniformity for operation at near-zero bias, high transimpedance linearity, and high staring FPA sensitivity.

The unit cell has a buffer amplifier consisting of CMOS inverter with high voltage gain (> 1000) and capability for operation at low power dissipation. The high gain yields excellent transimpedance linearity and a reduction in detector requirements. Near-zero detector bias and the concomitant low hybrid 1/f noise has thus been achieved. These translate to high quality imagery and obviate possible need for elaborate, space and power-consuming circuitry to suppress 1/f noise.

The readout is specifically designed for LWIR applications at large tactical backgrounds ($5 \times 10^{15} < Q_b < 2 \times 10^{17}$ photons/cm^2-sec). Flexibility has nevertheless been incorporated to enable high sensitivity at lower backgrounds. In addition, its extremely low input impedance and low input offset nonuniformity make it an ideal detector material assessment vehicle.

Input Circuit. Figure 26 is a block diagram of the ESBDI readout. With the exception of special features such as the detector clamp function and the use of distributed bus line capacitance, a classic BDI circuit is used with CMOS inverter amplifier. The open-loop voltage gain is about -1000 and the minimum power dissipation is 78 nW/cell. The minimum integration capacitor is provided by the bus line. Two MOS capacitors in the unit cell can be externally enabled. The ESBDI input circuit is configured for interface to detectors with *p*-on-*n* polarity.

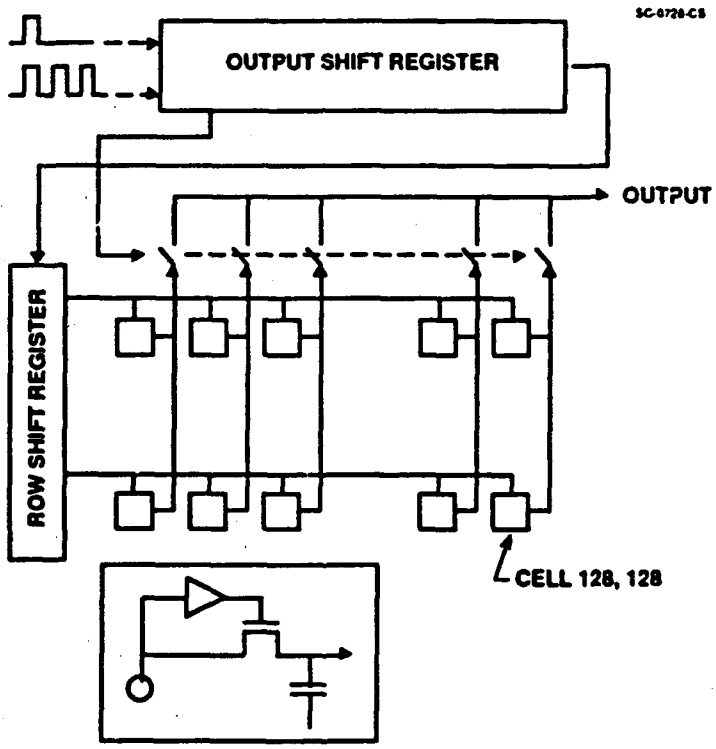

Fig. 26 Block Diagram of ESBDI readout.

The 128 x 128 has a pipelined switched-FET architecture with single output. The output circuit is comprised of a refined source follower design that has both 5 MHz data rate capability

and low noise (< 10 μV) to maintain a maximum dynamic range of 106 dB. Four external clocks are needed to operate the device. These include master clock, line sync, frame sync and bus access. The CMOS level (0 to 5V) clocks are buffered on-chip. The actual pixel multiplexing, reset, and access clocks are generated on-chip by static CMOS shift registers.

The ESBDI readout can be operated in either of two modes. In the "NORMAL" mode, the integration/frame time duty cycle is about 1/128. In this mode, the rows are read out sequentially for TV-compatible output. With "NORMAL" low, the readout duty cycle is nearly 1/64th, but the vertical information is output in a slightly scrambled sequence.

Readout Characteristics. Table 6 summarizes the characteristics of the ESBDI readout. The device has large charge-handling capacity, low input offset nonuniformity, and low input impedance across the intended range in photon backgrounds. Its capability for BLIP-limited sensitivity has yielded the highest LWIR sensitivity yet reported.[33]

Table 6
ESBDI Multiplexer Characteristics

Parameter	Value	Units
Nominal Supply Voltage	5.0	V
Minimum charge capacity	925	10^6 e-
Maximum Read Noise	1200	e-
Usable Dynamic Range	≥550	10^3
Maximum Data Rate	5	MHz
Maximum Input Offset Nonuniformity	<3	mV p-p
Readout Transfer Ratios	16.6 9.83 4.4	nV/e-

4.0 QWIP Hybrid FPA

4.1 Architecture

The hybrid FPAs consist of 128 × 128 GaAs/AlGaAs superlattice multiple quantum well detector arrays mated to high performance CMOS readouts. The quantum well infrared photodetector (QWIP) arrays were fabricated by AT&T Bell Laboratories in a complementary program through ARPA. Figure 27 shows cross sectional views of the hybrid FPA and the QWIP detector array. The former is fabricated at Rockwell Science Center, Thousand Oaks, CA; and the latter is fabricated by AT&T Bell Laboratories at the Solid State Technology Center, Breinigsville, PA.

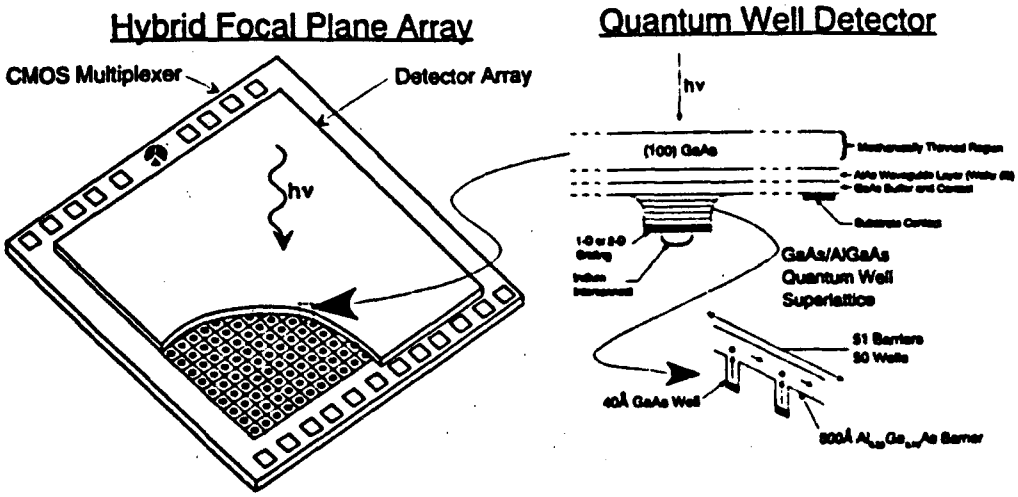

Fig. 27 Cross sectional illustrations of the hybrid focal plane array comprised of the detector array and the CMOS readout, and the quantum well infrared detector array.

The 128 × 128 hybrid FPAs were fabricated by mating silicon CMOS readouts to the GaAs-based detector arrays via indium interconnects. Interconnect yield is typically near-100%, but pixel yield was occasionally lower due primarily to column or row defects that were resident in the readout. Though the majority of readouts were screen-tested prior to hybridization and exhibited 100% functionality, some defects surfaced as a result of hybrid fabrication. These defects were believed a result of low quality overglass.

5.0 Hybrid FPA Performance

5.1 Impact of Optical Coupling Improvements

Radiometric tests of the QWIP focal plane arrays were performed at temperatures spanning the range from 30 to 82K. Optical response measured at 60K using a calibrated blackbody source at 900K under flood illumination indicated a peak responsivity for the arrays with 2-D gratings that is a factor of ~ 2 higher than that for the arrays with 1-D gratings. The peak responsivity for the arrays with 2-D gratings and AlAs waveguide layers is a factor of 8 to 15 times higher than that for the arrays with 1-D gratings. The typical measured responsivities corresponded to effective quantum efficiencies (ηC_p) of 1.0%, 2.3% and 15% at -2V bias (the top of the detector biased negative) for devices from layers 1195, 1242 and 1289, respectively. The best FPA from layer 1289 yielded mean ηC_p of ≈30% under flood illumination as shown in Fig. 28, a ηC_p histogram for Hybrid B-08.

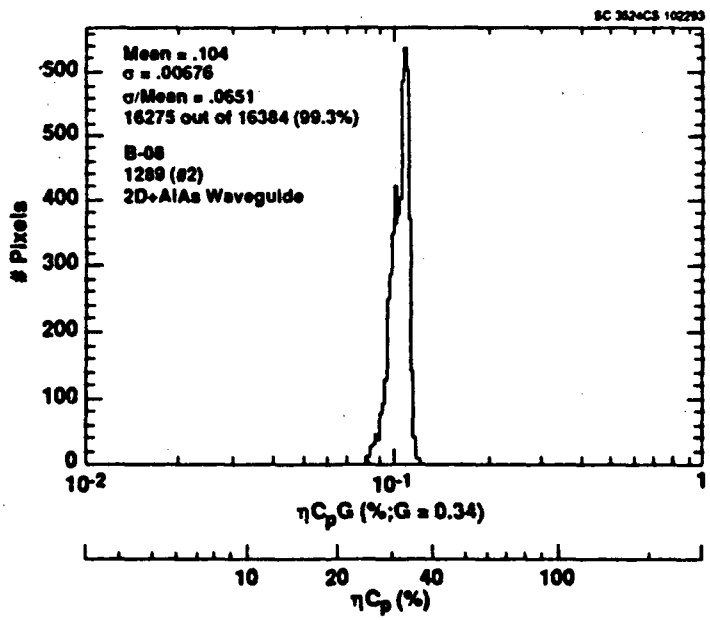

Fig. 28 Histogram of ηC_p and $\eta C_p G$ for Hybrid FPA B-08. Effective quantum efficiency of ≈30% was achieved.

Though over an order of magnitude improvement in responsivity was thus realized, optical scattering and reflection within the GaAs substrate resulted in unacceptable levels of crosstalk even with the devices having the highest coupling efficiency. Reconciliation of discrete detector test data prompted FPA-level experiments, which showed that the crosstalk often doubled the effective quantum efficiency across the array under flood illumination. Using focused spot illumination on arrays with 2-D optical grating and AlAs layer as evidenced in the array map shown in Fig. 29, 5% peak crosstalk was measured at the four primary lobes along both grating axes. The four peaks are roughly 15 pixels away from the primary signal in all four directions.

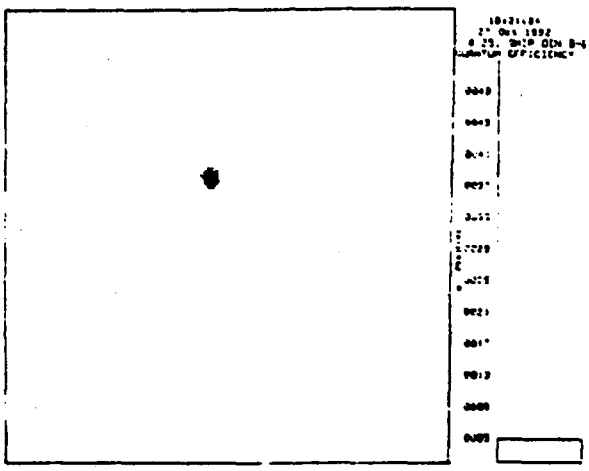

Fig. 29 Array Map for FPA B-08 showing optical crosstalk peaks of 5% along both axes of the 2-D optical grating for focused spot illumination.

We subsequently eliminated the crosstalk by thinning the completed FPAs using a diamond point lathe. This process reduced the effective quantum efficiencies by about 100% by eliminating the crosstalk signal. The final measured responsivities corresponded to effective quantum efficiencies (ηC_p) of 0.4%, 1.0% and 8% at -2V bias (the top of the detector biased negative) for layers #1195, #1242 and #1289, respectively.

The better results are summarized in Table 7 for thinned and unthinned FPAs. Though the highest effective quantum efficiency was achieved with unthinned devices having 2-D grating and optical cavity (i.e., AlAs waveguide layer), the best overall sensor performance was achieved on thinned devices having 2-D grating and optical cavity due to much lower optical crosstalk. The relative crosstalk is described in qualitative units since the actual values can vary greatly due to

experimental setup and apparatus. The thinned devices, however, have low crosstalk (< 3%) that is relatively independent of measurement conditions. The coupling improvements achieved in layers 1285 and 1286 were not as dramatic at the FPA level, though discrete detector measurements confirmed AT&T's results. The discrepancy has been ascribed to variation in the spectral characteristics of these two layers.

Table 7
QWIP FPA Quantum Efficiency

Detector Configuration	QWIP Wafer	Relative Crosstalk	Typical ηC_p (%)
1-D Grating	1195	Very High	1.0
2-D Grating	1242	High	2.3
2-D Grating and Optical Cavity	1289	High	15.0
Thinned with 1-D Grating	1195	Low	0.4
Thinned with 2-D Grating	1242	Low	1.2
Thinned with 2-D Grating and Optical Cavity	1289	Low	8.0

The peak spectral response for layers 1195, 1242 and 1289 typically showed peak wavelengths (λ_p) at 8.6 μm, 8.8 μm and 8.9 μm, respectively, even though the layers nominally had the same aluminum concentration. The slight variation in peak wavelength among the three wafers is caused by the spectral tuning of the gratings and waveguide layer. The 3 dB cut-off wavelength (λ_c) is approximately 9.5 μm for all three wafers.

The photoconductive gain, G, was determined from plots of the noise power spectral density versus total current at several low backgrounds and 40–60K operating temperatures. The maximum photoconductive gain varies between 0.2 and 0.4 for the three wafers at -2V, where the gain is often linear. Figure 30 shows the product $\eta C_p G$ as a function of the applied bias at the hybrid FPA level for a QWIP detector array from Layer #1289. Both prethinning and postthinning results are shown; thinning effectively reduces the effective quantum efficiency from 14% to 8% in trade for low crosstalk.

Another possible factor in QWIP detector bias optimization is uniformity. Figure 31 shows the impact on responsivity uniformity when the detector bias is increased from 0.8 V to 1.4 V. The product of ηC_p times the optical gain, G, increases as expected from 0.44% to 0.78% for a hybrid FPA (B-03) having 1-D grating. The effective quantum efficiency remains constant at about 1%, but the optical gain increases from 0.12 to 0.21. However, the rms nonuniformity also increases

from 2.76% to 4.0%. Though excellent for an LWIR 128 x 128 FPA, the higher nonuniformity reduces the available dynamic range.

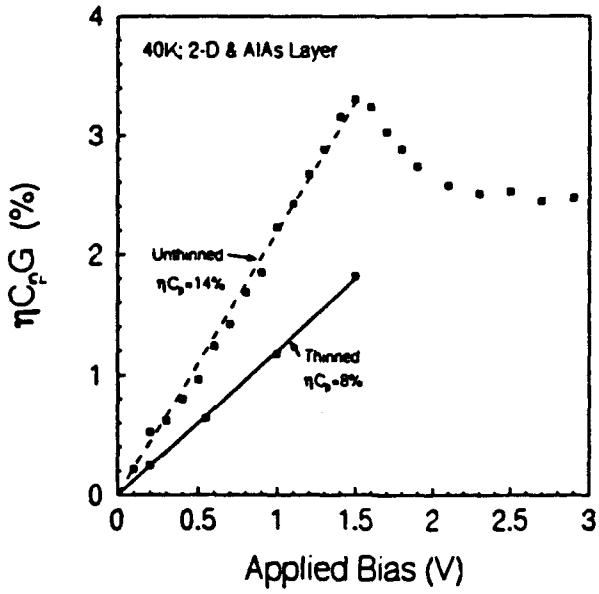

Fig. 30 Photoconductive gain vs. detector bias for layer 1289.

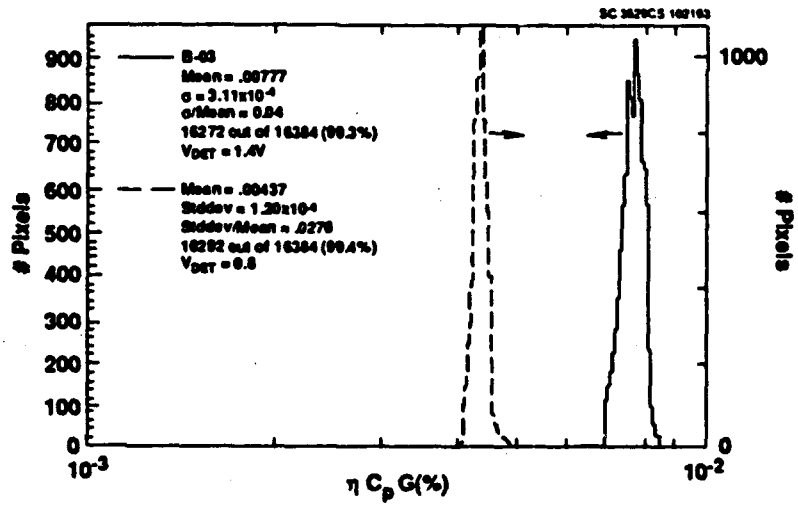

Fig. 31 Histograms of ηC_pG for Hybrid B-03 with 1-D lamellar grating at 0.8 V and 1.4 V bias.

5.2 Low Background

The QWIP FPA evaluation was initiated using a hybrid from layer 1195 (1-D grating; unthinned). Figure 32 shows the histograms of the peak detectivities measured at 1.29 x 10^{10} photons/cm^2-s background and both 40K and 35K operating temperatures. The D* is detector-limited at 40K to 61% of BLIP with a mean value of 3.68 x 10^{13} cm-Hz$^{1/2}$/W (the D* unit cm-Hz$^{1/2}$/W is often alternately referred to as Jones, after R.D. Jones, who introduced the concept of detectivity) and standard deviation of 30.4% relative to the mean. Reducing the temperature to 35K increased the mean D* to 4.51 x 10^{13} Jones and reduced the rms variation to 17.7%. The latter D* corresponds to 75% of BLIP for the measured FPA-level ηC_p of about 4.0% under flood illumination.

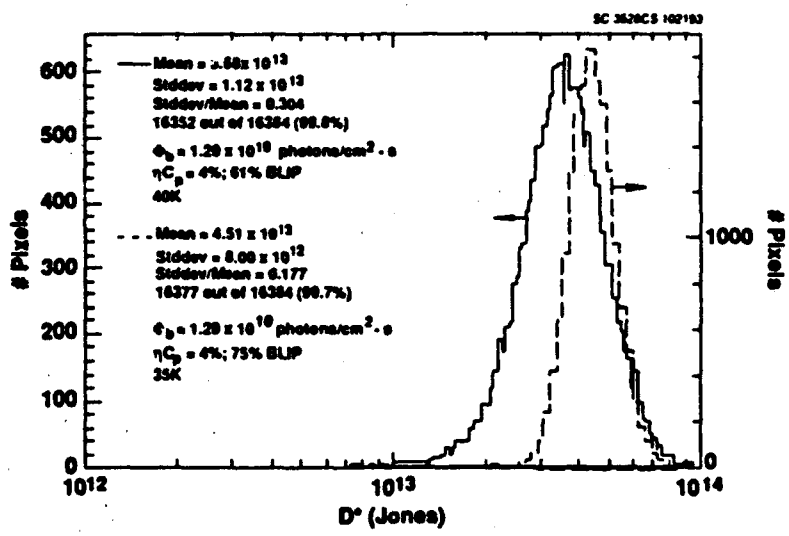

Fig. 32 Peak D* histograms at 40K and 35K operating temperatures for QWIP FPA from wafer #1195 at 1.29 x 10^{10} photons/cm^2-s background.

The measured D*'s and a comparison of the measured (≈ 34,000) gate modulation current gain to the theoretical value imply very low QWIP detector dark current of ≤ 0.3 fA at 2V bias and 40K operating temperature. The D* uniformity improved by ~ 70% at the lower operating temperature due to dark current suppression. The uncorrected response uniformity for this array is ~ 4%. Significant improvement in D* was not achieved in subsequent tests at lower background due to the relatively low effective quantum efficiency and the inability to operate the CMOS

multiplexer below about 32K (i.e., the multiplexer was not specifically optimized for deep cryogenic operation).

The FPA-level measurements corroborate and improve the discrete detector measurements. Figure 33 shows the discrete current-voltage (I-V) traces from layers 1195 (a) and 1242 (b) measured on discrete 200 μm x 200 μm detectors at zero degree field of view with the detectors looking at 20–30K background. The dark current at low bias voltages (-2 to +2V) is limited by the measuring instrument; the extremely low dark current prompted the assessment at low photon backgrounds and operating temperatures.

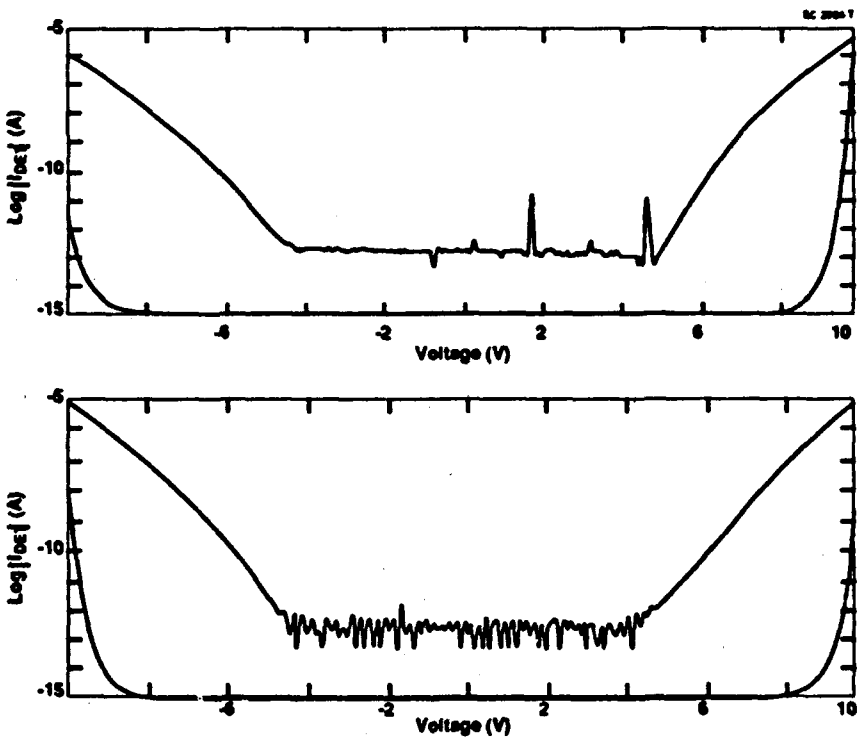

Fig. 33 Current-Voltage traces from layers 1195 (a) and 1242 (b) measured at zero degree field-of-view with the detector looking at 20–30K background.

Figure 34 is a histogram of the peak D* measured at 1.68 x 10^{11} photons/cm^2-s background and 40K temperature with a hybrid using a detector array from layer 1242 (2-D grating; unthinned). The mean of 1.44 x 10^{13} Jones is about 55% of BLIP for the measured FPA-level ηC_p of about 9.2% under flood illumination. Further tests at lower background revealed that

the FPA performance was detector-limited at roughly this level with roughly order-of-magnitude higher dark current than layer 1195. The uncorrected response uniformity for this array is ~ 3%.

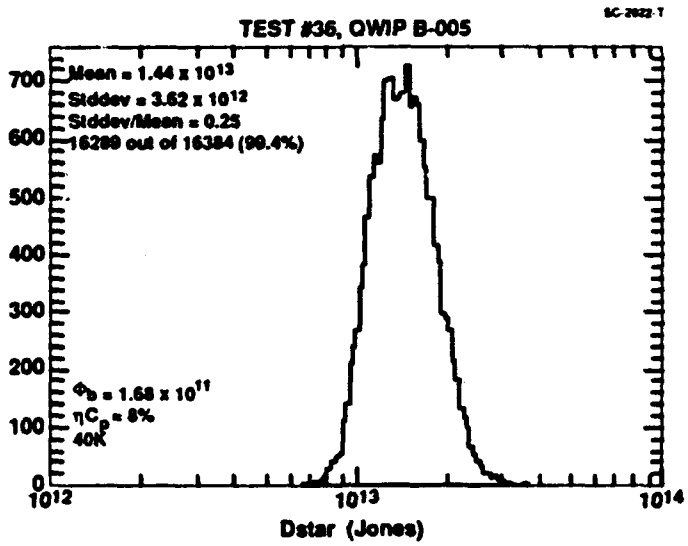

Fig. 34 Histogram of the peak D* measured at 1.68×10^{11} photons/cm^2-s background and 40K temperature. The QWIP array is from layer 1242.

We concluded the low background evaluation using a QWIP array from layer 1289 (2-D grating and AlAs waveguide layer; mechanically thinned). The thinned FPA yielded the highest performance yet reported with a QWIP staring FPA. Figure 35 is a histogram of the peak D* measured at 3.0×10^9 photons/cm^2-s background and 32.5K temperature. The mean D* is 9.96×10^{13} Jones with rms variation of 8.8% relative to the mean. The D* corresponds to about 80% of BLIP for the measured ηC_p of about 8.0% under flood illumination. The thinned FPA exhibited negligible crosstalk and generally excellent target detector characteristics including pixel operability of 99.3%. The measured D*'s and a comparison of the measured gate modulation current gain to the theoretical value imply very low QWIP detector dark current of $\leq 80 \times 10^{-18}$ A at 2V bias and 32.5K operating temperature.

Summarized in Fig. 36 are the key low background measurements. Layer 1289 yielded the QWIP FPA with the lowest dark current and highest post-thinning quantum efficiency; a D* of 10^{14} Jones was consequently achieved at the lowest background of 3×10^9 photons/cm^2-s. This result is consistent with the trend line for 10% effective quantum efficiency. A layer 1195 FPA

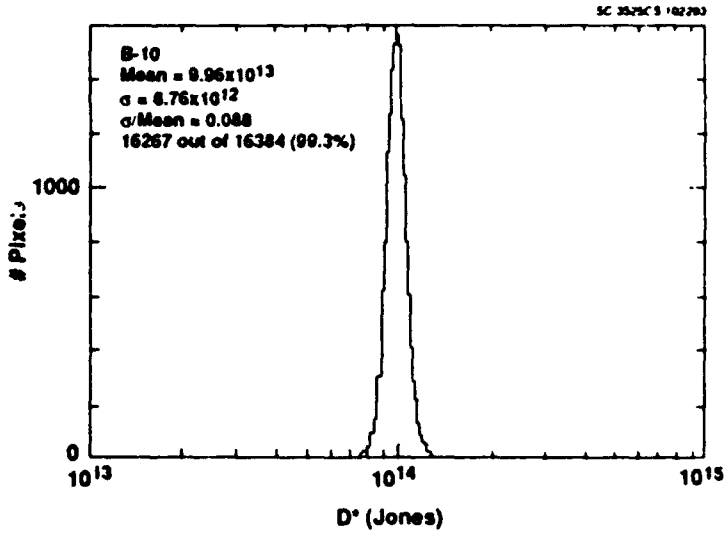

Fig. 35 Histogram of the peak D* measured at 3.0 x 10^9 photons/cm^2-background and 32.5K temperature (Thinned; Layer 1289).

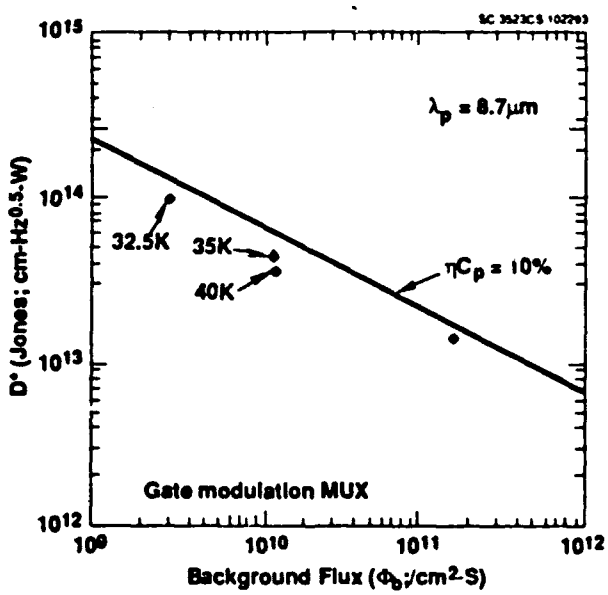

Fig. 36 D* vs. background flux.

produced the next highest D* approaching the aforementioned performance trend line, but the device was not thinned and exhibited relatively high crosstalk. The D* for a layer 1242 QWIP FPA saturated at slightly above 10^{13} Jones due to higher detector dark current.

5.3 FPA Performance at Conventional Imaging Backgrounds

5.3.1 Layer 1195 FPA Performance

The hybrids from QWIP layer 1195 generally exhibited BLIP sensitivity at temperatures below 65K, but the sensitivity at tactical temperatures (80K ± 2K) was detector-limited and inadequate for use in second generation IR sensors due to excess dark current. Table 8 summarizes the QWIP FPA performance and also lists the salient parameters gathered from the testing. Key parameters of note, in addition to the D*, are the effective quantum efficiency of up to 4%, maximum photoconductive gain of 0.324 at 2.14V, extremely low 1/f noise, and BLIP NEΔT of 0.014K measured at 60K.

Table 8
Lot 1 QWIP FPA Performance

Parameter	Value	Units
Background Flux	1.95×10^{16}	photons/cm^2-s
Detectivity @ 60K	1.12×10^{10}	Jones
%BLIP @ 60K	≈100	%
BLIP NEΔT f/1.6; 50Hz	0.014	K
Detectivity@ 80K±3K	$1.4\text{-}3.02 \times 10^{9}$	Jones
%BLIP @ 80K±3K	10-40	%
NEΔT @ 80K±3K f/1.6; 50 Hz	0.04-0.12	K
ηC_p	3.95	%
PC Gain	0.324	@ 2.14V
Spatial Noise	<0.1	%
1/f Noise @ 78K	<10	fA/Hz$^{1/2}$
1/f Noise @ 60K	<<1	fA/Hz$^{1/2}$
Pixel Operability	>98.5	%

The 8.7 μm hybrids were tested at unfiltered backgrounds determined by an f/1.6 cold shield and operating temperatures between 53K and 78K. Several important QWIP FPA

parameters thus determined include the product of coupling efficiency and quantum efficiency (ηC_p), photoconductive gain versus detector bias, and detectivity versus bias. While the internal quantum efficiency of the quantum well detectors is about 20%, the quantum well selection rule dictates that the coupling efficiency, C_p, can be much less than unity for light at normal incidence if optical gratings are not used and can be strongly dependent on the f/#. Assuming that is 20%, as is often observed in beveled (45°) discrete detectors, the coupling efficiency of the Lot 1 QIP detectors with one-dimensional gratings is estimated to be roughly 20% at f/1.6.

The PC gain was calibrated as a function of detector bias. We determined that the maximum photoconductive gain is about 0.35. The gain has the same bias dependency witnessed on prior devices and is linear for biases < 2.2V where:

$$PC\ Gain = 0.1512(V_{bias}) \tag{8}$$

Though PC gain was ascertained independent of temperature, operational considerations for full frame rate staring FPAs operating at TV-compatible frame rates dictate that more gain can be extracted as the temperature is lowered below 78K. The maximum readout charge-handling capacity of about 1.5 x 10^8 carriers corresponds to a maximum input current (for 50% fill) of about 375 pA at the nominal 22.5 msec integration time used for this characterization. This constraint works in conjunction with the detector Johnson noise to limit the sensor detectivity at low bias at 78K. The sensitivity of these 8.7 µm hybrids is Johnson noise-limited up to biases of 0.4 V at 77K and 0.6 V at 82K. Since the maximum allowable biases for full frame integration were roughly 150 mV and 30 mV, respectively, large D* dependence on temperature is implied. Plotted in Fig. 37 is the measured peak D* versus 1000/T. The highest D* was 3 x 10^9 Jones at 77K (Fig. 38). The D* degradation at higher temperatures agreed with the activation energy of 0.138 eV determined from discrete diode measurements.

D* optimization at 78K required shortening the integration time to enable application of sufficient bias for achieving g-r limited sensitivity. However, this degrades the NEΔT. Figure 39 is a histogram of the g-r limited D* at 77K. The mean of 7.80 x 10^9 Jones was measured at an integration time of 510 µsec.

While the full-frame 77K D* was limited by Johnson noise to roughly 40% of the achievable g-r limited sensitivity shown in Fig. 40, respectable NEΔT of 0.04 K was measured with excellent uniformity and yield of nearly 99%.

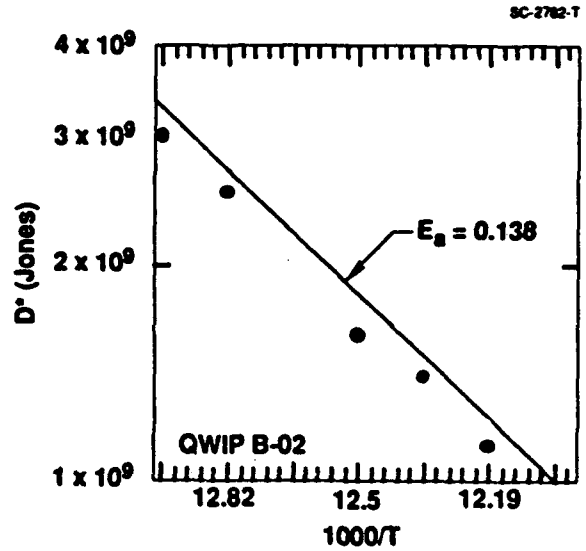

Fig. 37 D* vs. 1000/T for tactical operating temperatures and 22.5 ms integration time.

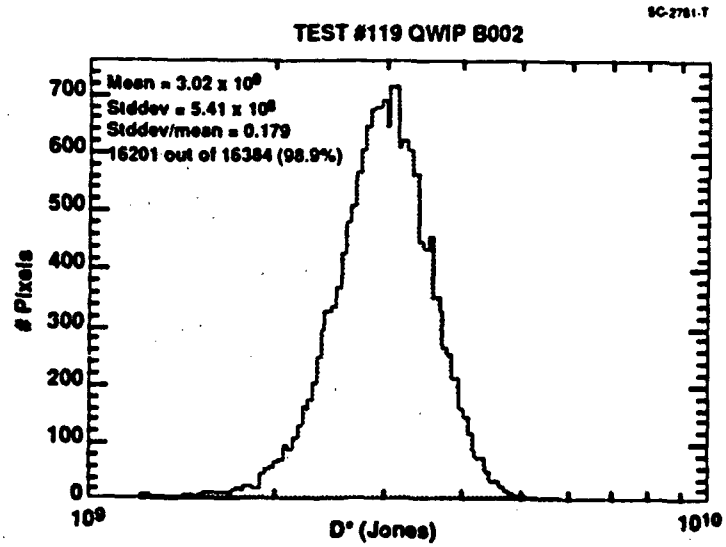

Fig. 38 D* at 22.5 msec integration time and 77K operating temperature.

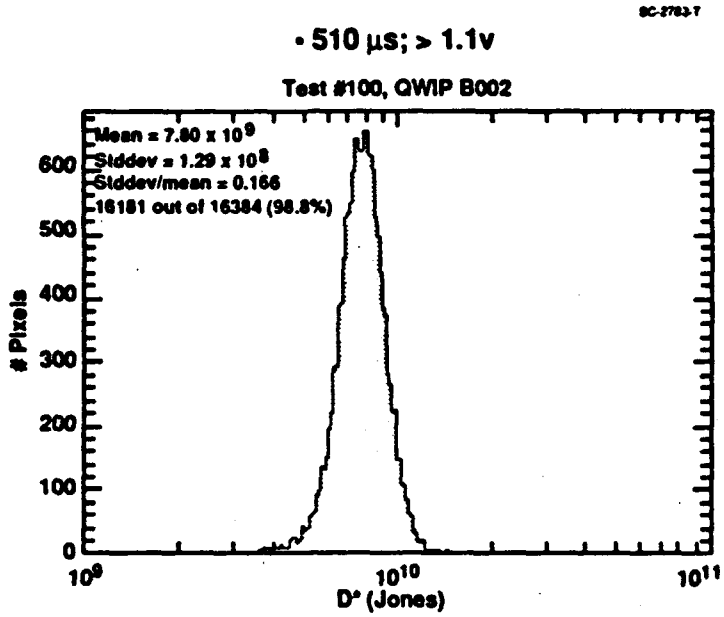

Fig. 39 G-R limited D* at 77K (510 µs integration time).

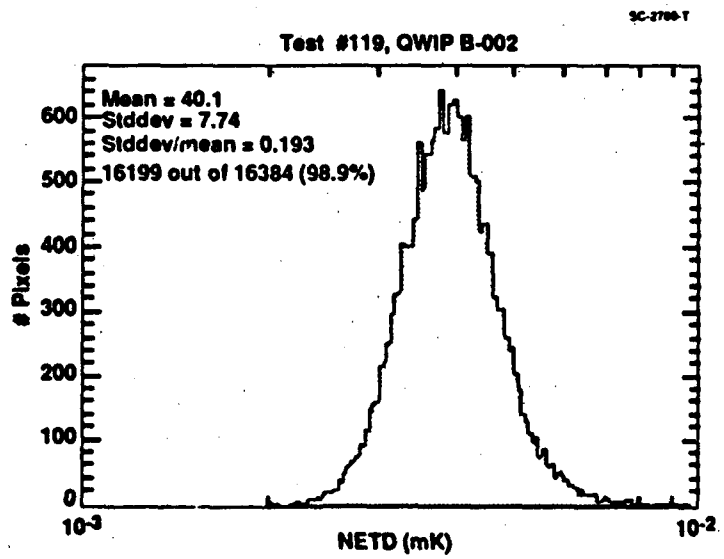

Fig. 40 Johnson noise limited NEΔT at 77K and 22.5 msec integration time.

All three hybrids exhibited similar sensitivity, particularly at temperatures below 70K. Hybrid B-001 was not tested below 77K due to an accident that resulted in dewar window

implosion and subsequent device failure. Figure 41 shows the BLIP D* achieved at 60K with Hybrid B-002. The distribution is tight with an rms nonuniformity of only 12.4%, even though only 30 frames were used to quantify pixel noise. The corresponding NEΔT under f/1.6 illumination is shown in Fig. 42. The mean is 0.0137K, and the operability is 98.4%. Table 9 succinctly compares the three hybrids.

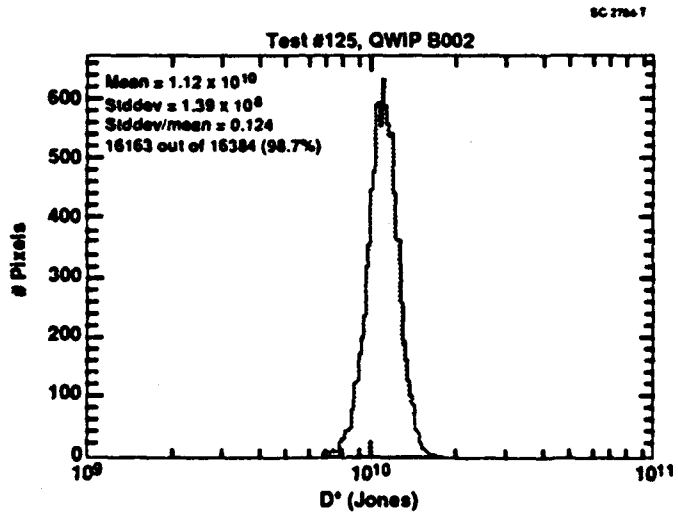

Fig. 41 BLIP D* for Hybrid B-002 (1.5 x 10^{16} photons/cm^2-s background).

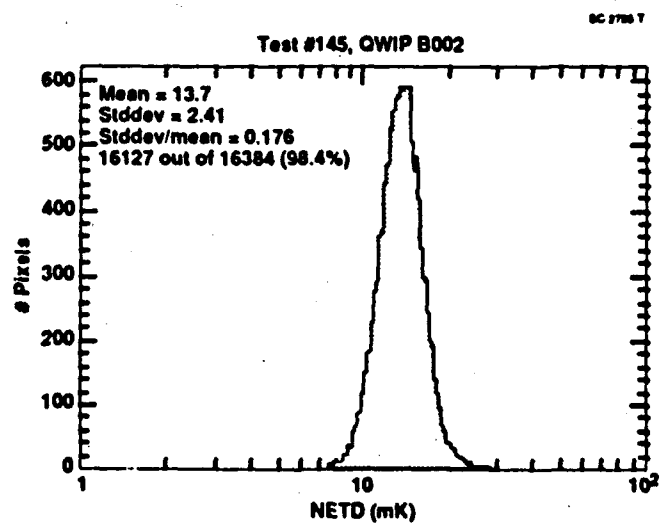

Fig. 42 BLIP NEΔT for f/1.6 illumination and ~ 50 Hz frame rate.

Table 9
Lot 1 QWIP FPA Performance Summary

DEVICE	ηC_p	OPERABILITY	BLIP D*
B-001	0.038	99.4	-
B-002	0.039	99.1	1.16×10^{10}
B-003	0.038	99.1	1.14×10^{10}

The three hybrids were very similar, differing only with respect to responsivity nonuniformity. The measured nonuniformity agreed with the grades assigned by AT&T based on characterization of the optical gratings. Figure 43 shows the $\eta C_p G$ uniformity of Hybrid B-002, which shows rms nonuniformity of 5.3% and a bimodal distribution stemming from geometrical nonuniformity in the gratings. The device had been graded "B"-quality by AT&T. The best uniformity was achieved with grade "A" hybrid B-003. Figure 44 shows a low bias $\eta \cdot C_p \cdot G$ nonuniformity of only 2.7% rms at 0.8 V bias. Table 10 compares the ratio of mean (σ) to standard deviation (μ) at 78K and 60K for the three hybrids.

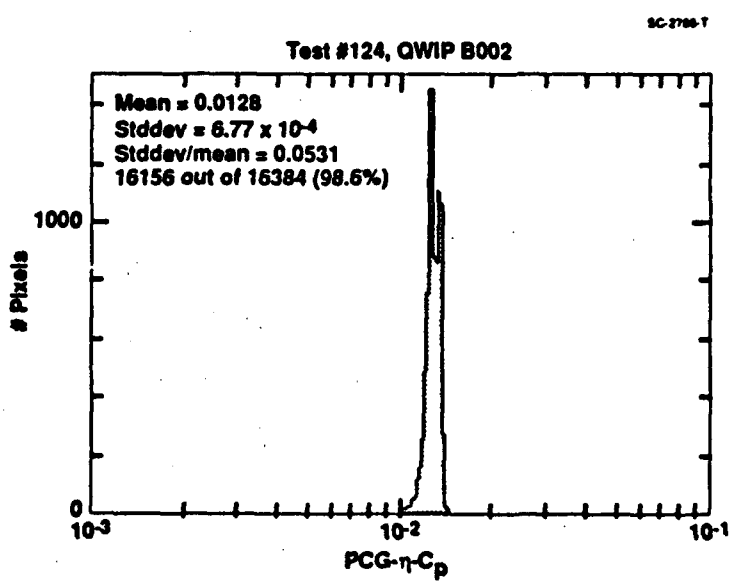

Fig. 43 $\eta \cdot C_p \cdot G$ nonuniformity for Grade "B" Hybrid B-002.

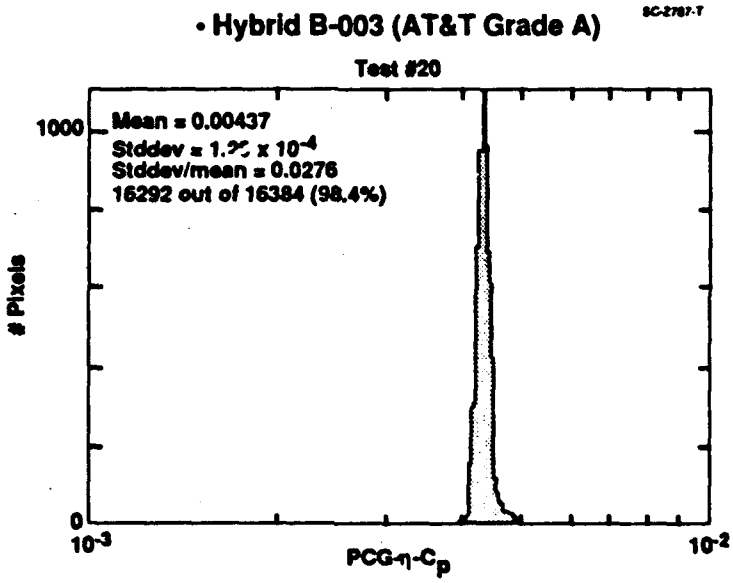

Fig. 44 η·Cp·G nonuniformity at 0.8V for Grade "A" Hybrid B-003.

Table 10
Lot 1 QWIP FPA Nonuniformity

GRADE: DEVICE	σ/μ at 78K	σ/μ at 60K
C: B-001	25%	-
B: B-002	15%	5.2%
A: B-003	12%	2.7%

Though excellent uniformity was achieved at low bias, some bias-dependent degradation was observed. Figure 45 shows the nonuniformity of hybrid B-003 at 1.4 V bias. The nonuniformity has increased from 2.7% rms to 4.3% rms. The uniformity is still quite good and translates to extremely large staring LWIR FPA usable dynamic range of over 84 dB.

FPA 1/f noise was generally negligible. Compared in Table 11 is the QWIP 1/f to state-of-the-art HgCdTe results. The 1/f is lower than the difference in quantum efficiency would imply. The negligible level of 1/f noise was corroborated by the imagery and the low D^* nonuniformity.

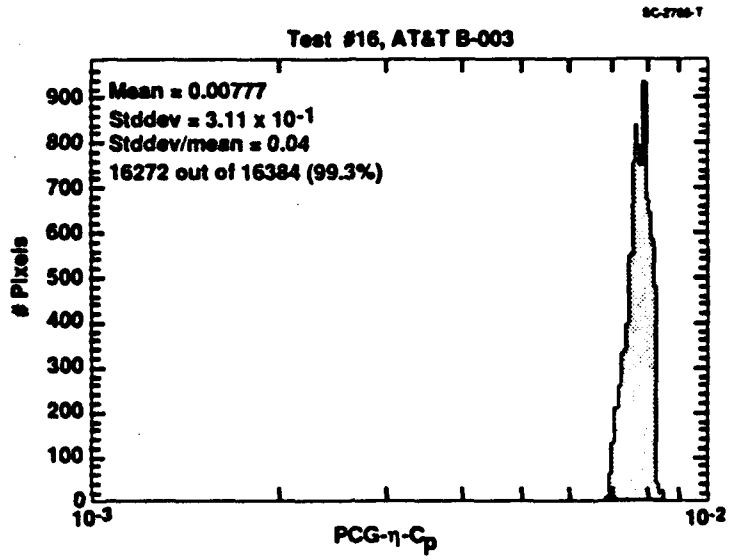

Fig. 45 $\eta \cdot C_p \cdot G$ nonuniformity at 1.4 V for Grade "A" Hybrid B-003.

Table 11
Detector 1/f Noise Comparison

TEMPERATURE	LPE HgCdTe	AT&T QWIP	UNITS
78K	30-100	7.6	$fA/Hz^{1/2}$
60K	-	<1	$fA/Hz^{1/2}$
40K	0.3-2	-	$fA/Hz^{1/2}$

Imaging Demonstration. Imagery generated with all three QWIP hybrids yielded good sensitivity and reasonable aesthetics. The main problem limiting the imagery was the optical crosstalk arising from internal reflections off the gratings. The principal reflections are vertical and occur in both directions at roughly 10 pixels from the illuminated element. The peak signal intensity of the first order reflection is 5.4% of the illuminated pixel, and the total reflected signal covers a fairly broad region as shown in Fig. 46, an array map generated during spot testing of hybrid B-002. To more clearly show the reflected signal, a ~ 3 x 3 element spot was used in this case. Though not discernible in the array map, the peak second order reflection is roughly 0.3% and is even more diffuse than the first-order reflection.

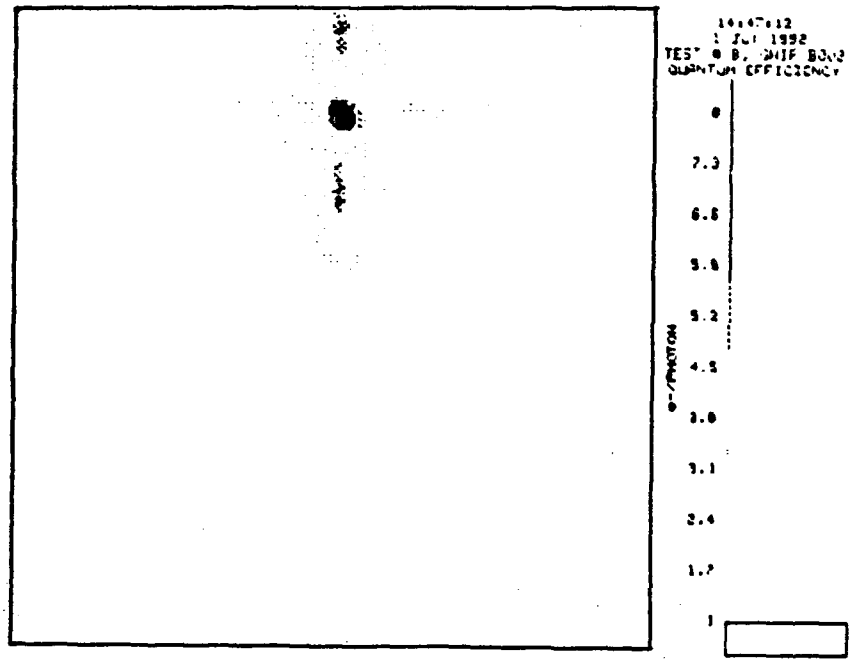

Fig. 46 Array map showing crosstalk pattern for spot scan illumination.

The performance improvements incorporated into the Lot 1 QWIP hybrids represented a significant improvement relative to prior art devices. Table 12 compares the Layer 1195 devices with previously fabricated QWIPs. The detector and readout improvements yielded 6X improvement in NEΔT at 78K.

Table 12
FPA Performance Summary at 78K

Parameter	Lot 1 8.7 μm QWIP	Prior 8.7 μm QWIP	Units
Format	128 x 128		Pixels
Cell Pitch	60		μm
Optical Interface	1-D Grating	Grating	
Typical Usable DR	85.2	84.9	dB
Maximum Usable DR	86.0	86.0	dB
Maximum Charge Capacity	16.5	9.25	10^7 carriers
Minimum NEΔT @ f/1.6; 78K	0.040	0.240	K
Minimum NEΔT @ f/1.6; 54K	0.014	0.018	K
Maximum D^* @78K, f/1.6	3.02	0.5	10^9 cm-Hz$^{1/2}$/W
Maximum D^* @60K, f/1.6	1.14	1.02	10^{10} cm-Hz$^{1/2}$/W
Responsivity Nonuniformity	<1.2:1	<2.0:1	Max:Min
Pixel Operability	>98	>98	%
Outputs	1		
Maximum Pixel Rate	5		MHz
Transfer Ratio	28	35	nV/e-

5.3.2 Impact of Optical Coupling Improvements

The improved quantum efficiency achieved with the 2-D grating and AlAs layer yielded enhanced sensitivity at conventional imaging backgrounds. Figure 47 is a histogram of the peak D* measured at 1 x 10^{16} photons/cm^2-s background and 60K temperature with hybrid B-08, which uses a layer 1289 QWIP (2-D grating; unthinned) and the high capacity direct injection multiplexer previously used (10^8 carrier charge-handling capacity). The mean of 8.08 x 10^{10} Jones is essentially BLIP for the measured ηC_p of ~ 15% under flood illumination. The uncorrected response uniformity for this array is ~ 5% and is limited by nonuniformity in the coupling efficiency due to variations in the optical gratings and the waveguide layer efficacy. Thinning a similarly configured FPA subsequently reduced the effective quantum efficiency by roughly a factor of two, resulting in slightly lower mean D* that is background limited to about 6 x 10^{10} Jones for temperatures < 62K. The imaging performance of the thinned hybrid was excellent, with mean NEΔT of 8.8 mK (Fig. 48), low crosstalk and pixel operability of 99.7%.

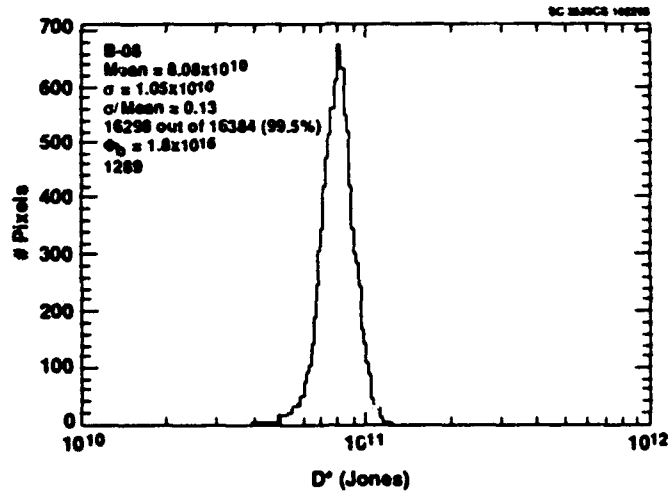

Fig. 47 D* histogram obtained at 1 x 10^{16} photons/cm^2-s background and 60K temperature. The QWIP array is from wafer #3.

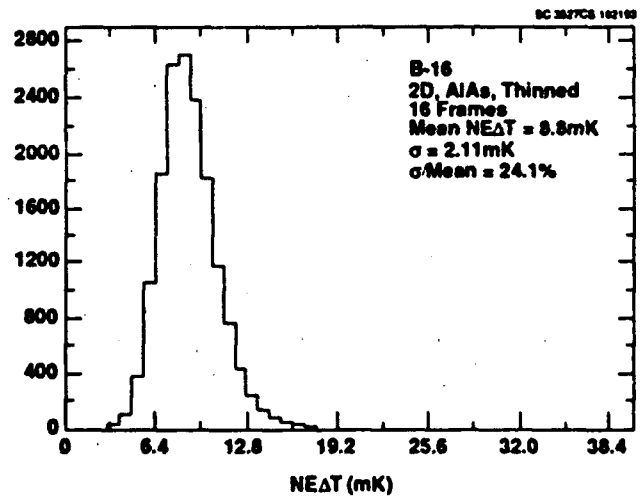

Fig. 48 NEΔT histogram generated at 1 x 10^{16} photons/cm^2-s background and 60K temperature. The thinned QWIP array is from wafer #3.

Figure 49 summarizes FPA measurements taken at higher backgrounds on several QWIP FPAs in the configurations earlier described. The higher backgrounds enabled easier attainment of BLIP sensitivity; the various D*'s are commensurate with the appropriate BLIP limits for the external quantum efficiencies that were achieved. The mechanically thinned devices with AlAs waveguide layer offer the best combination of D* and low optical crosstalk; these QWIP FPAs generated detectivities consistent with quantum efficiency of about 10%.

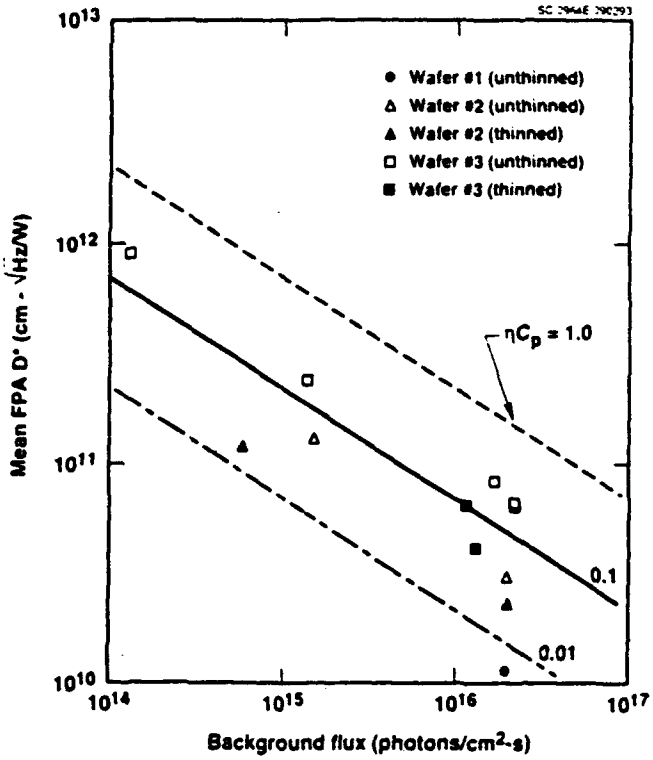

Fig. 49 Mean D* vs. background flux at 40K for several thinned and unthinned hybrids using detector arrays from layers 1195 (#1), 1242 (#2) and 1289 (#3).

6.0 FPA Test Methodology

6.1 Test Plan

FPA testing consisted of a set of standard tests performed at a variety of integration times. The tests included:

- rms noise (128 frame analysis)
- responsivity
- peak detectivity
- NEΔT
- effective quantum efficiency
- inferred detector R_0A product
- readout transimpedance
- pixel noise spectra (via FFT)

Not all the tests were performed on all the hybrids. Excess test station noise early in the test effort required that additional tests be performed to localize noise sources and help assess device limitations. Once device-limited sensitivity was achieved, testing focused on the minimum number of tests required to evaluate detector quality.

Basic testing consisted of measurement of pixel noise on an array basis via calculation of the standard deviation over 128 frames; the measurement of signal for a known input fluence from an extended-area blackbody; and the resultant detectivity calculation. The detectivity was calculated from the expression:

$$D^* = \frac{SIGNAL_i}{NOISE_i} \times D^*_{Factor} \qquad (9)$$

The detectivity conversion factor is:

$$D^*_{Factor} = \frac{1}{2A_{det}\,\tau_{int}}\,\frac{\lambda_{pk}}{hc\Delta\Phi} \tag{10}$$

and the input fluence used to determine the signal response is defined as:

$$\Delta\Phi = \frac{\tau_{cf}\,\tau_{dewar}}{44f/\#^2+1}\int_{\lambda_1}^{\lambda_2}\Phi_\lambda\,d\lambda \tag{11}$$

where τ_{cf} and τ_{dewar} are the average transmissions for the cold filter and dewar window, respectively.

NEΔT was measured on all of the hybrids using a methodology similar to that used for measuring D^*. After measuring rms noise and signal, the NEΔT was calculated using the expression:

$$NE\Delta T_i = \frac{NOISE_i}{SIGNAL_i\,\Delta\Phi}\left(\frac{\partial T}{\partial\Phi_{300K}}\right) \tag{12}$$

In actual practice, the software first calculates the NE, then translates this quantity to NEΔT by determining the incremental temperature equivalent at 300K. Thus, the calculated NEΔT is correct independent of the ΔT used to measure the signal.

6.2 Test Station Electronics

Figure 50 is a block diagram of the FPA test setup used to apply power and test the 18 QWIP hybrids. Figure 51 is a schematic of the typical electronics. Since a minimum of ground noise is critical, a previously designed and fabricated interface electronics box was used which is nominally located close to the dewar to ensure a localized ground. This electronics box consists of six clock drivers and eight dc bias supplies. The clock drivers are opto-isolated from the TTL-level Interface Technology RS-422 clock generator via HP 2631's. Teledyne TSC427 clock drivers are used to drive the clock signals. The three critical bias supples, GMODS, DLOAD, and DSUB, are derived from a precision 10 V reference (Burr-Brown REF102) which is buffered by a chopper stabilized operation amplifier (TI TLC2654) that is heavily filtered.

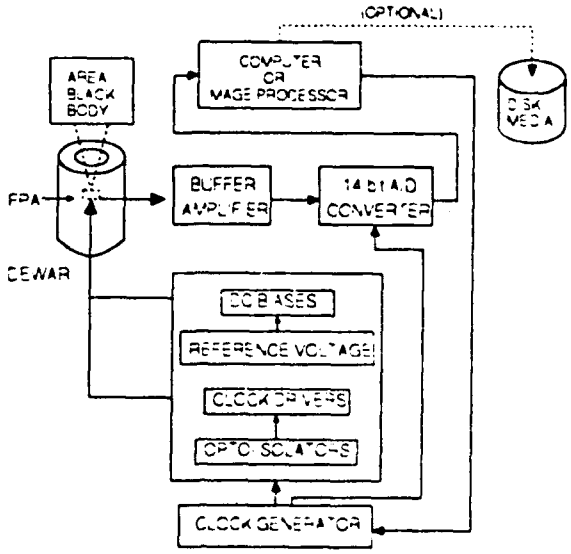

Fig. 50 FPA test setup.

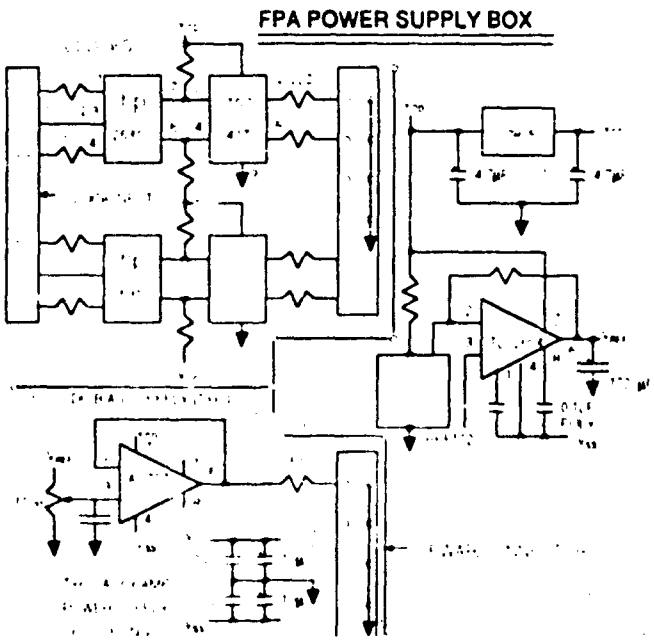

Fig. 51 Interface electronics (typical schematic).

The dewar and driver box ground scheme tries to minimize the ground impedance via multiground wires and braided cables. We believed that establishing a very good rf ground was more important than worrying about the associated ground loops, since the interface electronics is relatively close (electrically and position) to the FPA.

The FPA outputs were typically loaded with a 1 KΩ resistor pulled down to -5V and buffered by a multistage, amplifier chain with about 10 MHz bandwidth. The first stage amplifier uses a National LH0032 operational amplifier, while the second uses a National 6361 amplifier. Total gain for the two stages was typically in the range of 1 to 45, depending on test requirements. Maximum gain-stage noise was typically less than 10 μV.

Digitization was generally performed using a Burr Brown ADC614. The 5 MHz, 14-bit A/D typically offers about 12.5 effective number of bits in our custom electronics. Digital output is streamed to a frame buffer capable of storing 128 frames of 128 x 128 by 16-bit information. A few tests were performed using an alternate 12-bit A/D converters from Burr Brown (ADC603). Output from the frame buffer memory is ported to a Gateway 486/66 computer with extensive software support including FFT for calculation of noise spectra.

Table 13
Gate Modulation Readout: Interface Electronics

Name	Function	Typical Level (V)	Comments
V_{DD}, PWELL, DRAIN, ENABLE, V_D	Readout Supply Voltage	6	
GMODS	Input FET Source	~5.4	Adaptive Control
DSUB	Detector Substrate	6.7	Adaptive Control
CAP	Capacitor Plate	-0.5	
COLRST	Column Reset	1.2	
DLOAD	Load Fet Source/ Detector Load	2	
V_{RST}	Input FET Drain-Reset	0	
V_{SS}, VNEG	Ground	0	
MIRROR	Current Mirror Bias	200μA	Supplied by V_{DD}
CLOCK	Master Clock	0⇔5	
LSYNC	Line Synch	0⇔5	
FSYNC	Frame Synch	0⇔5	

7.0 QWIP FPA Cost Summary

In this report we consider the cost of the multiplexers, hybrid fabrication and hybrid test. The actual cost of QWIP detector arrays is covered in the AT&T report. The current cost of a prototype hybrid FPA similar to those fabricated in this program is estimated to be < $4000; production cost for large quantitites (hundreds or more) would be lower.

Analysis of the costs incurred over the course of the IR&D multiplexer development effort undertaken in FY 1988 incurred a cost of approximately $735 per multiplexer through indium bump deposition as outlined in Table 14. This cost reflects a relatively large markup in that the IR&D multiplexer development involved the sharing of four designs per wafer as shown in Fig. 52. Though this reduced the nonrecurring cost in accordance with one of our IR&D objectives, this inflates the recurring cost for the multiplexers from each design since much more handling is required. Specifically, each wafer contains only one-quarter of the possible number of devices of each design. Four-inch wafers were used since device count was not a driver for the IR&D effort. Each wafer must be tested, quartered and processed separately through indium deposition. Batch processing for In and pad metal deposition should drop the wafer processing cost significantly. Similarly, batch cryogenic testing of the FPAs can reduce the cost significantly. Finally, the IR&D effort was a low volume endeavor using highly skilled personnel.

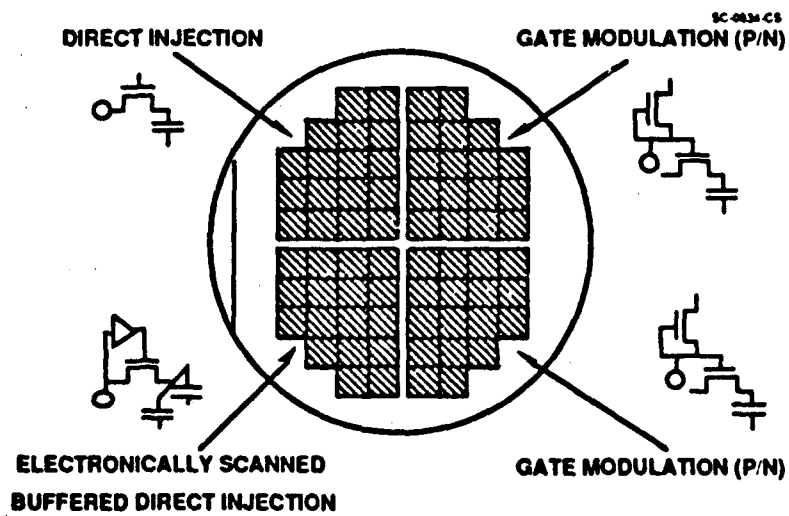

Fig. 52 IR&D 128 x 128 multiplexer wafer floor plan showing the four devices developed simultaneously in fiscal year 1988.

Table 14

QWIP FPA Cost Analysis

Item	Item Cost ($)	Unit Cost ($)
Multiplexer Fabrication	475	
MUX Wafer Probe Test	10	
Wafer Processing (Indium & Pad Metal)	200	
MUX Die Test	50	735/MUX
Hybridization	100	100/FPA
Cryogenic FPA Test	1500	1500/FPA
Data Pack	100	100/FPA
Total Cost Not Including QWIP Array	2435	2435
Estimated Total Cost per QWIP FPA	< 4000	< 4000

The multiplexer cost was driven for this task by the cost of the prototype lot of 4-inch wafers. Table 15 outlines the typical yield for one of the four IR&D 128 x 128 multiplexer designs. The catalog cost at Orbit Semiconductor for the 2 μm process is $27,000 for delivery of ≥ 5 wafers. The final cost of a yielded CMOS readout is hence < $800 for this small prototype lot. Analysis of recent development costs suggests that the multiplexer cost can be easily reduced to < $100 per readout. Focusing on one device per wafer increases parts count by 400% and similarly reduces cost; similarly, fabricating on 5" wafers increases parts counts and reduces cost by an additional 250%.

The cost of cryogenic testing assumes the use of senior MTS labor and can also be drastically reduced in production. The cost includes tasks that can otherwise be handled by technicians including dewar preparation and cooldown. If the temperature range for testing is limited to temperatures compatible with LN2, the cost can be halved.

Table 15

IR&D 128 x 128 Readout: Typical Functional Yield

Wafer #	High Quality Die	% Yield
906T119-01	6/14	43
906T119-02	1/13	7
906T119-04	4/14	28
906T119-05	1/13	7
906T119-09	2/13	15
906T120-01	6/14	43
TOTAL	20/71	28

8.0 References

1. M.T. Asom, M.W. Focht, W.A. Gault, K.G. Glogovsky, G. Guth, R.E. Leibenguth, G. Livescu, L.C. Luther, J.W. Stayt, Jr., V. Swaminathan, Y.M. Wong, C.G. Bethea, T.R. Fullowan, B.F. Levine, A. Zussman, J. Blackwell, W. Parrish, L.J. Kozlowski, K. Vural and G.M. Williams, "A Description and Video Demonstration of a LWIR 128x128 GaAs/$Al_xGa_{1-x}As$ Multiple Quantum Well Detector Hybrid," IRIA-IRIS Proceedings 1991 Meeting of the IRIS Specialty Group on Infrared Detectors, Volume 1, *13-16*, August 1991 (Infrared Information Analysis Center, ERIM, Ann Arbor, MI, Dec. 1991) p. 13.

2. L.J. Kozlowski, R.E. DeWames, G.M. Williams, S.A. Cabelli, K. Vural, D.T. Cheung, and W.E. Tennant, C.G. Bethea, B.F. Levine, W.A. Gault, K.G. Glovsky and J. W. Stayt, Jr., "LWIR 128x128 GaAs/AlGaAs Multiple Quantum Well Hybrid FPA Assessment and Comparison to HgCdTe," *ibid*, p. 29.

3. B.F. Levine, C.G. Bethea, G. Hasnain, V.O. Shen, E. Pelve, R.R. Abbott and S.J. Hsieh, Appl. Phys. Lett. *56*, 851 (1990).

4. J.Y. Anderrson, L. Lundqvist and Z.F. Paska, Appl. Phys. Lett. *58*, 2264 (1991).

5. J.Y. Anderrson and L. Lundqvist, Appl. Phys. Lett. *59*, 857 (1991).

6. B.K. Janousek, M.J. Daugherty, W.L. Bloss, M.L. Rosenbluth, M.J. O'Loughlin, H. Kanter, F.J. DeLuccia and L.E. Perry, J. Appl. Phys. *67*, 7608 (1990).

7. S.D. Gunapala, B.F. Levine, L. Pfeiffer and K. West, J. Appl. Phys. *69*, 6517 (1991).

8. S.R. Andrews and B.A. Miller, J. Appl. Phys. *70*, 993 (1991).

9. K.K. Choi, M. Dutta, P.G. Newman, M.L. Saunders and G.J. Iafrate, Appl. Phys. Lett. *57*, 1348 (1990).

10. C.G. Bethea, B.F. Levine, V.O. Shen, R.R. Abbott and S.J. Hsieh, IEEE Trans. Electon Dev. *38*, 1118 (1991).

11. L.J. Kozlowski, G.M. Williams, G.J. Sullivan, C.W. Farley, R.J. Anderson, J. Chen, D.T. Cheung, W.E. Tennant and R.E. DeWames, "LWIR 128x128 GaAs/AlGaAs Multiple Quantum Well Hybrid Focal Plane Array," IEEE Trans Electron Dev. *38*, 1124 (1991).

12. B.F. Levine, S.D. Gunapala and R.F. Kopf, Appl. Phys. Lett. *58*, 1551 (1991).

13. H. Schneider, F. Fuchs, B. Dischler, J.D. Ralston and P. Koidl, Appl. Phys. Lett. *58*, 2234 (1991).

14. A. Zussman, B.F. Levine, J.M. Kuo and J. deJong, J. Appl. Phys. *70*, 5101 (1991).

15. B.F. Levine, C.G. Bethea, K.G. Glogovsky, J.W. Stayt, Jr. and R.E. Leibenguth, Semicond. Sci. Technol. *6*, C114 (1991).

16. B.F. Levine, A. Zussman, J.M. Kuo and J. de Jong, (unpublished).

17. A. Köck, E. Gornik, G. Abstreiter, G. Böhm, M. Walther and G. Weimann, Semicond. Sci. Technol. *6*, C128 (1991).

18. L.J. Kozlowski, G.M. Williams, R.E. DeWames, J.W. Stayt, Jr., V. Swaminathan, K.G. Glogovsky, R.E. Leibenguth, L.E. Smith, and W.A. Gault, "128 x 128 GaAs/AlGaAs QWIP Infrared Focal Plane Array with Background Limited Sensitivity at 40K," submitted for publication.

19. V. Swaminathan, J.W. Stayt Jr., J.L. Zilko, K.D. C. Trapp, L.E. Smith, S. Nakahara, L.C. Luther, G. Livescu, B.F. Levine, R.E. Leibenguth, K.G. Glogovsky, W.A. Gault, M.W. Focht, C. Buiocchi and M.T. Asom, IRIA-IRIS Proceedings, 1992 Meeting of the IRIS Specialty Group on Infrared Detectors, Aug. 1992, Moffet Field, CA.

20. R.E. DeWames, J.M. Arias, L.J. Kozlowski, and G.M. Williams, "An assessment of HgCdTe and GaAs/AlGaAs technologies for LWIR infrared imagers," SPIE Vol. 1735, (1992).

21. J.Y. Anderrson, L. Lundqvist and Z.F. Paska, Appl. Phys. Lett. *58*, 2264 (1991).

22. J.Y. Anderrson and L. Lundqvist, Appl. Phys. Lett. *59*, 857 (1991).

23. V. Swaminathan, J.W. Stayt Jr., J.L. Zilko, K.D. C. Trapp, L.E. Smith, S. Nakahara, L.C. Luther, G. Livescu, B.F. Levine, R.E. Leibenguth, K.G. Glogovsky, W.A. Gault, M.W. Focht, C. Buiocchi and M.T. Asom, IRIA-IRIS Proceedings, 1992 Meeting of the IRIS Specialty Group on Infrared Detectors, Aug. 1992, Moffet Field, CA.

24. L.J. Kozlowski, G.M. Williams, G.J. Sullivan, C.W. Farley, R.J. Anderson, J. Chen, D.T. Cheung, W.E. Tennant and R.E. DeWames, "LWIR 128 x 128 GaAs/AlGaAs Multiple Quantum Well Hybrid Focal Plane Array," IEEE Trans. Electron Devices, Vol. 38, No. 5, May 1991.

25. L.J. Kozlowski, G.M. Williams, K. Vural and W.E. Tennant, "Performance of a 128 x 128 Staring MWIR HgCdTe PACE-1 Hybrid Focal Plane Array at TE-cooled Temperatures," 1990 National IRIS, Johns-Hopkins University, Laurel MD, 12-14 June 1990.

26. L.J. Kozlowski, G.M. Williams, G.J. Sullivan, C.W. Farley, R.J. Anderson, J.K. Chen, D.T. Cheung, W.E. Tennant, and R.E. DeWames, "LWIR 128x128 GaAs/AlGaAs Multiple Quantum Well Hybrid Focal Plane Array," IEEE Trans. on Electron Devices, Vol. 38, No. 5, May 1991.

27. L.J. Kozlowski, S. A. Cabelli, D.E. Cooper and K. Vural, "Low Background Infrared Hybrid Focal Plane Array Characterization," SPIE Vol. 1946, (1993).

28. L.J. Kozlowski, J.M. Arias, R.E. DeWames, K. Vural, J.G. Pasko, A.B. Vanderwyck and W.E. Tennant, "MBE LWIR PV HgCdTe Staring FPA Assessment," Proceedings of the IRIS Specialty Group on Infrared Detectors, NIST, Boulder, CO,, 13-16 August 1991.

29. L.J. Kozlowski, S.L. Johnston, W.V. McLevige, A.H.B. Vanderwyck, D.E. Cooper, S.A. Cabelli, E.R. Blazejewski, K. Vural and W.E. Tennant, SPIE Vol. 1685, April 1992.

30. L.J. Kozlowski, W.V. McLevige, A.H. Vanderwyck, D.E. Cooper, S.L. Johnson, K. Vural and W.E. Tennant, Proceedings of the IRIS Specialty Group on Infrared Detectors, NIST, Boulder, CO,, 13-16 August 1991.

31. L.J. Kozlowski, S. A. Cabelli, D.E. Cooper and K. Vural, "Low Background Infrared Hybrid Focal Plane Array Characterization," SPIE Vol. 1946, (1993).

32. N. Bluzer and R. Stehlik, "Buffered Direct Injection of Photocurrents into Charge-Coupled Devices," IEEE Journal of Solid-State Circuits, Vol. SC-13, No. 1 February 1978.

33. J.M. Arias, L.J. Kozlowski, J.G. Pasko, M. Zandian, S.H. Shin, R.E. DeWames and W.E. Tennant, "MBE LWIR HgCdTe PACE-II Focal Plane Arrays," IRIS Detector Specialty Group Proceedings, NIST, Gaithersburg, MD, 14-16 August 1990.